

## Movement-Robust mmWave VR via Dual-Beam Reception and Predictive Beam Transition

Hersyandika, Rizqi; Xiong, Haoqiu; Miao, Yang; Wang, Qing; Pollin, Sofie

**DOI**

[10.1109/OJCOMS.2025.3556761](https://doi.org/10.1109/OJCOMS.2025.3556761)

**Publication date**

2025

**Document Version**

Final published version

**Published in**

IEEE Open Journal of the Communications Society

**Citation (APA)**

Hersyandika, R., Xiong, H., Miao, Y., Wang, Q., & Pollin, S. (2025). Movement-Robust mmWave VR via Dual-Beam Reception and Predictive Beam Transition. *IEEE Open Journal of the Communications Society*, 6, 2420-2437. <https://doi.org/10.1109/OJCOMS.2025.3556761>

**Important note**

To cite this publication, please use the final published version (if applicable). Please check the document version above.

**Copyright**

Other than for strictly personal use, it is not permitted to download, forward or distribute the text or part of it, without the consent of the author(s) and/or copyright holder(s), unless the work is under an open content license such as Creative Commons.

**Takedown policy**

Please contact us and provide details if you believe this document breaches copyrights. We will remove access to the work immediately and investigate your claim.

# Movement-Robust mmWave VR via Dual-Beam Reception and Predictive Beam Transition

RIZQI HERSYANDIKA<sup>1</sup> (Graduate Student Member, IEEE), HAOQIU XIONG<sup>1</sup> (Student Member, IEEE),  
YANG MIAO<sup>1,2</sup> (Senior Member, IEEE), QING WANG<sup>3</sup> (Senior Member, IEEE),  
AND SOFIE POLLIN<sup>1,4</sup> (Senior Member, IEEE)

<sup>1</sup>Department of Electrical Engineering, KU Leuven, 3000 Leuven, Belgium

<sup>2</sup>Department of Electrical Engineering, University of Twente, 7522 NB Enschede, The Netherlands

<sup>3</sup>Department of Software Technology, Delft University of Technology, 2628 CD Delft, The Netherlands

<sup>4</sup>Interuniversity Microelectronics Centre, 3001 Leuven, Belgium

CORRESPONDING AUTHOR: R. HERSYANDIKA (e-mail: rizqi.hersyandika@kuleuven.be)

This work was supported by the Smart Networks and Services Joint Undertaking (SNS JU) under the European Union's Horizon Europe Research and Innovation Programme under Grant 101096954 (6G-BRICKS) and Grant 101139291 (iSEE-6G).

**ABSTRACT** The abundant bandwidth in the mmWave band supports high data rates and low latency communication, making it ideal for delivering realistic and seamless virtual reality experiences. However, a key challenge lies in adapting the mmWave beams to the highly dynamic user movements, which often cause beam misalignment, resulting in signal degradation and potential outages. Additionally, maintaining uninterrupted signal reception during beam re-alignment due to head rotation requires low-overhead and timely beam transitions to prevent signal drops caused by delayed switching. This paper addresses these challenges with a joint solution at both the access point (AP) and head-mounted display (HMD) ends. Specifically, the proposed solution integrates coordinated multi-point networks with dual-beam reception at the HMD to enhance diversity, improve channel gain, and mitigate outages caused by user movement. Evaluation using real HMD movement datasets demonstrates that dual-beam reception within a coordinated multi-AP setup achieves up to a 22.8% improvement in reliability by reducing outage rates compared to single-beam reception. Experimental validation further highlights the effectiveness of combining widely distributed APs with a locally distributed subarray configuration on the HMD, improving angular coverage during head rotations. Furthermore, our predictive beam transition approach anticipates the future beam during user movements, preventing received signal degradation from delayed transitions while reducing overhead by 43.8% compared to exhaustive periodic beam searches.

**INDEX TERMS** mmWave, virtual reality, head-mounted device, multi-point networks, beamforming, beam prediction.

## I. INTRODUCTION

### A. MOTIVATION

IMMERSIVE virtual reality (VR) applications hold huge promise in various industries, including automotive, healthcare, education, and tourism. Achieving truly immersive experiences relies heavily on high-speed data transfer, which is crucial to rendering realistic environments, facilitating smooth interactions, and enabling seamless content streaming. Millimeter-wave (mmWave) frequency bands are well suited to meet these high-speed data transfer and low latency requirements thanks to the large

bandwidth available in mmWave bands [1]. For example, the IEEE 802.11ad standard supports a data rate up to 6.75 Gbps [2], enough for the needed wireless transmission of an uncompressed high-definition (1080p) video which requires a 4.5 Gbps data rate. Further enhancements in IEEE 802.11ay, including channel bonding, channel aggregation and multiple-input multiple-output (MIMO), promise data rates of up to 100 Gbps [3]. This satisfies the 64 Gbps data rate requirement for transmitting uncompressed 8K video at a 24 Hz refresh rate [4]. Nevertheless, communication in the mmWave bands faces challenges due to higher path loss

compared to lower-frequency bands, requiring beamforming gain compensation at both the transmission and the reception ends.

The nature of dynamic user head movements in VR applications can cause antenna and beam misalignment between the access point (AP) and head-mounted display (HMD), reducing the channel gain and making links unstable [5], [6]. Addressing these misalignments caused by head movements is crucial when operating VR applications in mmWave networks, where beamforming is essential at the APs and the HMD sides. Therefore, efforts on both sides are necessary to minimise link outage periods, reduce channel gain instability, and ensure smooth beam transition within the set of beams at each AP and HMD during misalignments caused by movement.

Deploying multiple APs around the HMD can effectively improve the link stability by providing a wider angular coverage, thereby reducing outages when an AP falls outside the HMD's field of view (FoV). The use of mmWave coordinated multi-point (CoMP) networks, as investigated in [7], improves reliability by providing spatial diversity to serve VR users. These networks mitigate single-link outages caused by user movement by transmitting the same stream through multiple spatially separated APs. Multiple transmit (Tx) beams can be generated either through spatially separated coordinated APs [8] or by a single AP transmitting two synchronised beams: a line-of-sight (LoS) beam and a reflected beam. When path delays are sufficiently compensated for, these two beams combine constructively in the user device [9]. In-band multi-connectivity networks with local analog beamforming for interference suppression eliminate the reliance on phase-coherent processing [10]. Other AP-side solutions include the integration of the mmWave network with legacy sub-6 GHz Wi-Fi as a backup mechanism [7], [11] and the use of free space optics for dual connectivity [12] to mitigate mmWave link outages.

To fully exploit the presence of multiple serving APs, the HMD must be capable to generate multidirectional beams to receive signals from multiple APs with high reception gain. Multibeam reception at the HMD can be achieved straightforwardly using hybrid beamforming, where multiple radio frequency (RF) chains control subsets of antenna elements to generate independent Rx beams directing towards different APs. As an alternative solution for a low-cost HMD equipped with a single RF chain, analog-based multibeamforming can be employed to generate multidirectional reception.

Other important features required on the HMD to minimise outages due to frequent and rapid head motions include beam re-alignment and beam-tracking. Data from the inertial measurement unit (IMU) sensor, commonly available in HMDs, can be leveraged for mmWave beam re-alignment and beam-tracking, making it applicable for VR applications [13], [14]. Several IMU-based HMD movement datasets, such as [6], [15], [16], [17], can be utilised to emulate the IMU-assisted beamforming and analyse the impact of HMD misalignment on communication performance. These data sets typically

consist of 6 degrees of freedom (6DoF) motion data sampled at specific intervals using HMDs, gathered from participants engaged in activities such as watching interactive VR videos or playing VR games.

Nevertheless, the sampling rate of IMU can vary across devices, making it challenging to standardise the beam re-alignment period. Any delay in delivering IMU data to the beamformer may result in a late beam transition, potentially degrading the received signal performance. Consequently, IMU-free predictive beam alignment approaches should also be considered. Exhaustive scanning, a common baseline approach, searches all codebook directions for optimal alignment but incurs high overhead, making it impractical for latency-sensitive VR applications. Compressed sensing beam alignment technique [18] reduces the number of beam measurements by exploiting the inherent sparsity of mmWave channels, at a high computational cost for recovering the sparse signals. Fingerprinting method [19] relies on pre-collected channel fingerprints, which may not generalise well to rapidly changing VR environments where user movement and blockage alter the propagation conditions. Sensor-assisted-based beam alignment approaches leveraging camera [20], LiDar [21] or sub-6-GHz channel [22] provide accurate tracking information but introduce additional hardware dependencies, that may not be practical for lightweight and power-constrained HMDs.

The predictive approach proposed in [23] employs an interleaved subarray on the HMD to generate a subbeam that proactively predicts the future angle-of-arrival (AoA) based on movement. However, this approach faces limitations due to mutual coupling effects caused by irregular element spacing within the subarray. Developing a predictive beam alignment solution that ensures smooth beam transitions while maintaining low beam training overhead remains an open challenge in this area.

Beam tracking algorithms have been proposed to maintain the mmWave beam alignment under user mobility. The works in [24], [25], [26] consider extended Kalman filter (EKF)-based beam tracking, while [27] proposes a fast beam training method combined with probabilistic beam tracking using hybrid transceivers. Several experimental evaluations of the mmWave beam tracking are presented in [28], [29], [30]. The work in [28] implements beam tracking by selecting the best neighbouring beam based on error vector magnitude (EVM) observations. Meanwhile, [29] and [30] utilise the 5G NR waveform structure and camera sensing, respectively, for beam tracking. However, these beam-tracking approaches are primarily designed to address mobility challenges in vehicular and outdoor environments, where translational movements are more dominant as opposed to rotational movements considered in this work.

In contrast to outdoor scenarios, the movement of a VR user is characterised by frequent and rapid rotational motions, primarily due to head rotations, where translational movement is less dominant. Apart from investigations into the impact of different array configuration on HMDs

conducted in [31], experimental research focusing specifically on mmWave communications for VR applications remain limited. This gap motivates us to conduct experimental investigations into both AP-side and HMD-side solutions aimed at enhancing robustness against user movement in mmWave VR applications.

## B. CONTRIBUTIONS

In this paper, we aim to improve the robustness of mmWave VR applications against frequent and rapid head movements. We propose solutions at both the AP and HMD ends to improve the channel gain, expand the HMD's FoV, minimise outage periods during head movements, and ensure smooth beam transitions in the event of misalignment. The detailed contributions of this paper are listed below.

- 1) We propose an analog dual-beam reception technique for low-cost mmWave HMDs with a single RF chain. Using a centrally placed uniform planar array (UPA), dual beams are formed by superimposing beamforming weight vectors targeting two coordinated APs, enhancing channel gain and reducing outages during frequent head movements in VR streaming.
- 2) We develop a beam misalignment model that translates 6DoF head movement into position displacement and angular misalignment in azimuth and elevation, enabling IMU-assisted beamforming for precise beam direction. Using real HMD movement datasets, we emulate the dynamic mmWave channel between serving APs and a moving HMD to analyse wireless communication performance.<sup>1</sup> Evaluation of dual-beam reception across various AP separation angles shows a reduction in outage rates by up to 22.8% compared to single-AP case with single-beam reception. However, a trade-off exists: wider AP separation improves rotation robustness but reduces receive (Rx) levels when the HMD aligns with the APs due to off-broadside beam steering.
- 3) We experimentally evaluate dual-connectivity performance in VR applications using our mmWave testbed, measuring mmWave channels between two spatially separated APs and a rotating HMD receiving the stream via two directional beams with hybrid beamforming employing two RF chains. We assess various AP separation distances and Rx subarray configurations on the HMD: co-located and locally distributed. Results show that increased AP separation and a locally distributed subarray improve FoV and reduce outage periods, achieving up to 11.3 dB higher minimum Rx signal levels compared to smaller AP separation with a co-located subarray.

<sup>1</sup>The development of the analog dual-beam reception for mmWave HMDs and the beam misalignment model builds on our prior work [32], which analysed a simulated 28 GHz channel using an HMD movement dataset from [15]. In this study, we extend the analysis to a 60 GHz environment and enhance VR use case diversity by incorporating datasets from both [15] and [6].

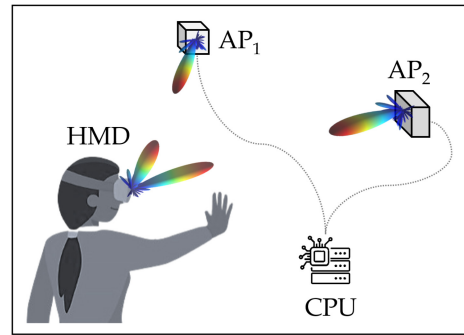


FIGURE 1. Dual-beam reception at HMD-VR in mmWave CoMP networks.

- 4) We propose a predictive beam transition mechanism that minimises Rx level drops due to late transitions. By analysing Rx level observations from neighbouring beams, this approach reduces scanning overhead and eliminates the need for IMU sensor input. The future beam is predicted by combining beam group correlations and Rx level gradients. Evaluation using our mmWave testbed shows that our approach predicts the future beam up to hundreds of milliseconds in advance, reducing Rx level drops compared to reactive 3-dB threshold and periodic re-alignment in IEEE 802.11ad/ay. It also cuts scanning overhead by 43.8% compared to exhaustive searches employed in the baseline approaches.

## II. COORDINATED MULTI-POINT AND ANALOG DUAL-BEAMFORMING RECEPTION

### A. CHANNEL MODEL

We consider mmWave CoMP networks to serve a mmWave user where multiple spatially distributed APs, coordinated by a central processing unit (CPU), cooperate to serve an HMD user using multiple directive Tx beams, as illustrated in Fig. 1. The HMD employs multiple directive Rx beams aligned with the Tx beam directions. For effective multibeam reception, it is crucial that the HMD receives signals from  $L$  serving APs that combine constructively.

We assume perfect channel estimation between the HMD and each serving AP, obtained through the uplink pilot transmission with directive beam used on both sides. The CPU collects and combines the estimated channels from all serving APs to determine the precoding vector for each AP,  $v_l$ , under the assumption of channel reciprocity in time division duplex (TDD). We focus on a single-user scenario, where maximum ratio transmission (MRT) precoding is sufficient to ensure constructive signal reception at the HMD. For scenarios involving multiple HMD users, more advanced precoding techniques such as zero-forcing (ZF) or minimum mean square error (MMSE), could be used to mitigate inter-user interference.

For downlink transmission, we consider dominant LoS paths between the HMD and serving APs. The received signals at the HMD represent the coherent summation of all

downlink signals transmitted from  $L$  serving APs, formulated as:

$$y^{\text{DL}} = \sum_{l=1}^L \sqrt{p_l} v_l h_l^{\text{DL}} s_d + z_k, \quad (1)$$

where  $p_l$  denotes the transmit power of AP- $l$ ,  $v_l$  is the precoding vector of AP- $l$ ,  $h_l^{\text{DL}}$  represents the complex downlink channel between AP- $l$  and the HMD,  $s_d$  is the transmitted data stream, and  $z_k$  denotes the additive white Gaussian noise at the HMD- $k$  with the noise figure of  $F_k$ .

The complex LoS downlink channel between AP- $l$  and the HMD includes the beamforming gain at both the AP and HMD, and can be expressed as:

$$h_l^{\text{DL}} = \frac{c}{4\pi f_c d_l} \sqrt{g_l^{\text{Tx}}(\theta_D, \phi_D) g^{\text{Rx}}(\theta_A, \phi_A)} e^{-j \frac{2\pi f_c d_l}{c}}, \quad (2)$$

where  $f_c$  denotes the carrier frequency,  $c$  represents the speed of light,  $d_l$  is the distance between the HMD and AP- $l$ ,  $g_l^{\text{Tx}}(\theta_D, \phi_D)$  denotes the Tx beamforming gain of AP- $l$  at the angle-of-departure (AoD) of  $(\theta_D, \phi_D)$ , and  $g^{\text{Rx}}(\theta_A, \phi_A)$  denotes the Rx beamforming gain of HMD at the angle of arrival (AoA) of  $(\theta_A, \phi_A)$ .

## B. BEAMFORMING WITH UPA

We consider a UPA $_{(M \times N)}$ , consisting of  $M$  horizontal elements and  $N$  vertical elements, used on each AP and HMD side. Assuming a half-wavelength spacing between the two horizontal and vertical elements, the array response vector of the  $(m, n)$ -th elements of UPA at the azimuth angle  $\theta$  and the elevation angle  $\phi$  is expressed as [33]:

$$a_{m,n}(\theta, \phi) = e^{-j\pi \sin \theta (m \cos \phi + n \sin \phi)}, \quad (3)$$

where  $m = \{0, \dots, M-1\}$  and  $n = \{0, \dots, N-1\}$ . The overall array response vector is denoted as  $\mathcal{A} \in \mathbb{C}^{1 \times MN}$ , where  $\mathcal{A} = \{a_{1,1}, \dots, a_{M,N}\}$ , assuming ideal array without gain and phase errors due to array imperfection.

To steer the beam toward a specific direction, a beamforming weight vector needs to be assigned to each element. The weight vector of the  $(m, n)$ -th element for steering the beam in the direction  $(\theta_b, \phi_b)$  can be defined as follows:

$$w_{m,n}(\theta_b, \phi_b) = e^{j\pi \sin \theta_b (m \cos \phi_b + n \sin \phi_b)}. \quad (4)$$

The overall beamforming weight vector of an array is denoted as  $\mathcal{W} \in \mathbb{C}^{1 \times MN}$ , where  $\mathcal{W} = \{w_{1,1}, \dots, w_{M,N}\}$ . The beamforming gain in the direction  $(\theta, \phi)$  given the beamforming direction  $(\theta_b, \phi_b)$  is then expressed as:

$$g(\theta, \phi, \theta_b, \phi_b) = |\mathcal{W}^T(\theta_b, \phi_b) \mathcal{A}(\theta, \phi)|^2. \quad (5)$$

The  $(\theta, \phi)$  direction corresponds to the AoD and AoA defined in (2).

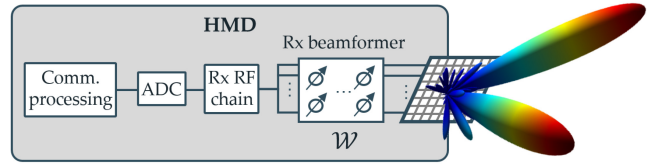


FIGURE 2. System architecture of analog dual-beam reception HMD.

## C. DUAL-BEAM RECEPTION AT THE HMD

The HMD employs dual beam reception based on analog beamforming to receive signals from multiple serving APs with strong gains, steering two directional Rx beams toward the APs' directions. Fig. 2 presents the system architecture of analog dual reception HMD, where each element is phase-controlled by the Rx beamformer connected to a single RF chain. The adjustment of the beamforming weight vector  $\mathcal{W}$  can be based on the beam training results or the input from IMU. These multidirectional beams can be generated using analog beamforming through two methods: *partitioned* and *combined* beamforming weight vector allocation.

### 1) PARTITIONED BEAMFORMING

In the partitioned beamforming method, the antenna array is divided into multiple subarrays, each assigned an independent beamforming weight vector to steer its beam toward a corresponding AP. This approach allows each subarray to direct its beam towards its target direction independently. The  $L$  beamforming weight vectors assigned by the partitioned beamformer to generate  $L$  directive beams can be expressed as follows:

$$\mathcal{W}_p = \{\mathcal{W}_1(\theta_1, \phi_1), \dots, \mathcal{W}_l(\theta_l, \phi_l), \dots, \mathcal{W}_L(\theta_L, \phi_L)\}, \quad (6)$$

where  $\mathcal{W}_p \in \mathbb{C}^{1 \times MN}$  and  $\mathcal{W}_l(\theta_l, \phi_l) \in \mathbb{C}^{1 \times MN/L}$ .  $\mathcal{W}_l(\theta_l, \phi_l)$  represents the individual beamforming weight vector allocated for the  $l$ -th subarray to generate a beam in the  $(\theta_l, \phi_l)$  direction, where  $\theta_l$  and  $\phi_l$  denote the azimuth and elevation angles of the desired beam direction, respectively. Alternatively, power division can also be controlled by dividing an unequal number of antenna elements.

### 2) COMBINED BEAMFORMING

In the combined beamforming method, all antenna elements are used to generate beams in multiple directions. This is accomplished by superimposing multiple beamforming weight vectors, each pointing toward the directions of the  $L$  serving APs. The combined beamforming weight vectors assigned by the beamformer to generate  $L$  directive beams can be expressed as:

$$\mathcal{W}_c = \frac{\sum_{l=1}^L \sqrt{\eta_l} \mathcal{W}_l(\theta_l, \phi_l)}{\sum_{l=1}^L |\sqrt{\eta_l} \mathcal{W}_l(\theta_l, \phi_l)|} \in \mathbb{C}^{1 \times MN}, \quad (7)$$

where  $\mathcal{W}_l(\theta_l, \phi_l) \in \mathbb{C}^{1 \times MN}$  denotes the beamforming weight vector of the UPA used to beamform towards the intended  $(\theta_l, \phi_l)$  direction, and  $\eta_l$  represents the power coefficient of beam  $l$ , with constraint  $\sum_{l=1}^L \eta_l = 1$ . Unlike the partitioned

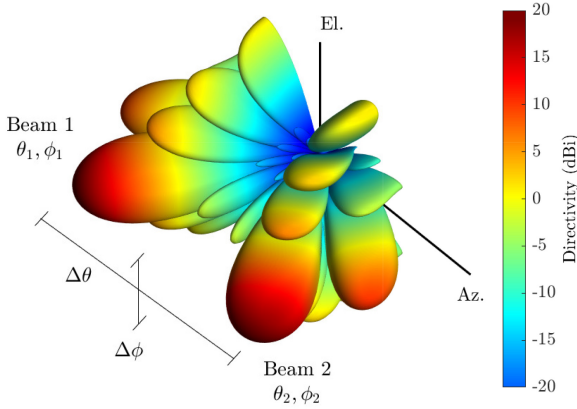


FIGURE 3. Example of analog dual-beam pattern for HMD reception.

method, which divides the power equally among subarrays, the parameter  $\eta_l$  in the combined beamforming method allows for the adjustment of the power between the beams, allowing for more flexible beamforming.

For both cases, the beamforming gain of the multi-beam configuration is obtained by substituting (6) or (7) into (5). Fig. 3 illustrates the beam pattern of dual beam ( $L = 2$ ), where the first beam is steered at  $(\theta_1, \phi_1)$  and the second beam is steered at  $(\theta_2, \phi_2)$ , generated using UPA<sub>(8×8)</sub> with the combined beamforming method. The separation in the azimuth and elevation directions is indicated as  $\Delta\theta = |\theta_2 - \theta_1|$  and  $\Delta\phi = |\phi_2 - \phi_1|$ , respectively. In this example, the power is equally shared between two beams with  $\eta_1 = \eta_2 = 0.5$ , resulting in identical beamforming gains,  $g(\theta_1, \phi_1) = g(\theta_2, \phi_2)$ , in both intended steering directions. Please note that this work does not address multibeam optimisation or beam quantisation. These aspects are studied in detail in [34].

### III. HEAD MOTION MODEL AND BEAM MISALIGNMENT

Misalignment between the AP(s) and the HMD can significantly impact communication performance, as the AoD and AoA are key parameters for evaluation. In this section, we derive these parameters as function of head movements that naturally occur in VR applications. The IMU sensor on the HMD typically provides a 6DoF metric, representing both translational and rotational head movements. This information is then utilised in IMU-based beam tracking to dynamically re-align the beam at the HMD in real-time.

#### A. TRANSLATIONAL MOVEMENT

The translational movement of an HMD not only changes the HMD–AP distance but also causes beam misalignment between them, since the positional displacement of the HMD changes its orientation with respect to the serving AP(s), as illustrated in Fig. 4(a). The positions of HMD- $k$  and AP- $l$  in Cartesian coordinates are denoted as  $P_k = [x_k, y_k, z_k]$  and  $P_l = [x_l, y_l, z_l]$ , respectively, which serve as the global reference coordinates for the scenario. The orientation vector

between HMD- $k$  and AP- $l$  in the spherical coordinate can be expressed as:

$$Q_{d,\theta,\phi} = [d_{kl}, \theta_{kl}, \phi_{kl}]. \quad (8)$$

$d_{kl}$  denotes the HMD–AP distance, while  $\theta_{kl}$  and  $\phi_{kl}$  represent the HMD's relative azimuth and elevation angles with respect to the AP, formulated as:

$$d_{kl} = \sqrt{(x_k - x_l)^2 + (y_k - y_l)^2 + (z_k - z_l)^2}, \quad (9)$$

$$\theta_{kl} = \arctan2\left(\frac{y_k - y_l}{x_k - x_l}\right), \quad (10)$$

$$\phi_{kl} = \arctan\left(\frac{(z_k - z_l)}{\sqrt{(x_k - x_l)^2 + (y_k - y_l)^2}}\right). \quad (11)$$

The arctan2 function in (10) takes into account the signs of  $(x_k - x_l)$  and  $(y_k - y_l)$  to determine the angle's quadrant, and thus provides an unambiguous result in the range  $[-\pi, \pi]$ .

Denoting the initial HMD- $k$ 's position as  $P_{k,x,y,z}^0 = [x_k^0, y_k^0, z_k^0]$  and the HMD's translational movement in the corresponding axis as  $[x', y', z']$ , the HMD- $k$ 's position after the translational movement can be expressed as:

$$P_{k,x,y,z}^{\text{trn}} = \begin{bmatrix} x_k^{\text{trn}} \\ y_k^{\text{trn}} \\ z_k^{\text{trn}} \end{bmatrix} = \begin{bmatrix} x_k^0 + x' \\ y_k^0 + y' \\ z_k^0 + z' \end{bmatrix}. \quad (12)$$

By substituting  $x_k^{\text{trn}}, y_k^{\text{trn}}, z_k^{\text{trn}}$  to  $x_k, y_k, z_k$  in (9), (10) and (11), the resulting HMD orientation vector after translational movement is written as:

$$Q_{d,\theta,\phi}^{\text{trn}} = [d_{kl}^{\text{trn}}, \theta_{kl}^{\text{trn}}, \phi_{kl}^{\text{trn}}]. \quad (13)$$

#### B. ROTATIONAL MOVEMENT

In the IMU sensor, the rotation of the device is represented by yaw, pitch, and roll movements, as depicted in Fig. 4(c). Yaw signifies left and right head rotations around the vertical  $z$ -axis (i.e., shaking the head), pitch indicates up and down head movements around the  $y$ -axis (i.e., nodding), and roll expresses head-tilt movements around the  $x$ -axis. These rotational movements can be expressed using the following Euler rotation matrix:

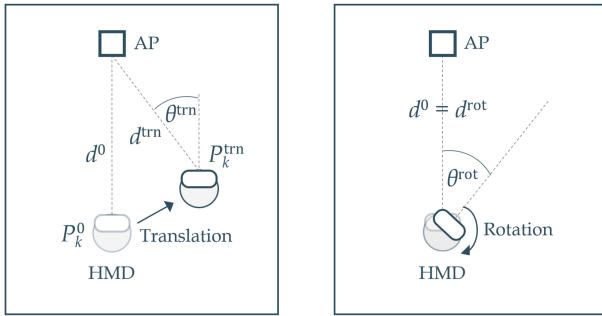
$$\mathcal{R}_x(\alpha) = \begin{bmatrix} 1 & 0 & 0 \\ 0 & \cos(\alpha) & -\sin(\alpha) \\ 0 & \sin(\alpha) & \cos(\alpha) \end{bmatrix}, \quad (14)$$

$$\mathcal{R}_y(\beta) = \begin{bmatrix} \cos(\beta) & 0 & \sin(\beta) \\ 0 & 1 & 0 \\ -\sin(\beta) & 0 & \cos(\beta) \end{bmatrix}, \quad (15)$$

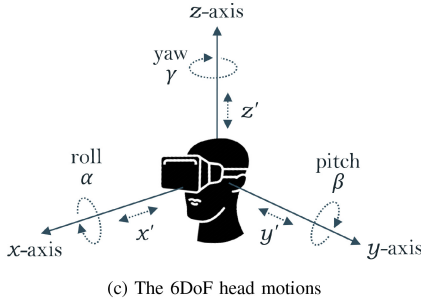
$$\mathcal{R}_z(\gamma) = \begin{bmatrix} \cos(\gamma) & -\sin(\gamma) & 0 \\ \sin(\gamma) & \cos(\gamma) & 0 \\ 0 & 0 & 1 \end{bmatrix}, \quad (16)$$

where  $\alpha$ ,  $\beta$ , and  $\gamma$  correspond to roll, pitch, and yaw movements, respectively. Following the XYZ convention rotation, the rotation matrix becomes:

$$\mathcal{R} = \mathcal{R}_x(\alpha)\mathcal{R}_y(\beta)\mathcal{R}_z(\gamma). \quad (17)$$



(a) Translational movement (b) Rotational movement



(c) The 6DoF head motions

FIGURE 4. Illustration of HMD movements in the  $x - y$  plane and the 6DoF head motions.

To apply the Euler rotation matrix, the orientation in spherical coordinates  $(Q_{d,\theta,\phi})$  must first be converted to Cartesian coordinates,  $Q_{x,y,z} = [q_x, q_y, q_z]$ , where:

$$q_x = d_{kl} \cos(\theta_{kl}) \cos(\phi_{kl}), \quad (18)$$

$$q_y = d_{kl} \sin(\theta_{kl}) \cos(\phi_{kl}), \quad (19)$$

$$q_z = d_{kl} \sin(\theta_{kl}). \quad (20)$$

Then, the rotated orientation vector in the Cartesian coordinate becomes:

$$Q_{x,y,z}^{\text{rot}} = Q_{x,y,z} \mathcal{R}, \quad (21)$$

where  $Q_{x,y,z}^{\text{rot}} = [q_x^{\text{rot}}, q_y^{\text{rot}}, q_z^{\text{rot}}]$ . The orientation vector after HMD rotation is converted back to the spherical coordinate following:

$$Q_{d,\theta,\phi}^{\text{rot}} = \begin{bmatrix} \sqrt{q_x^{\text{rot}2} + q_y^{\text{rot}2} + q_z^{\text{rot}2}} \\ \arctan2(q_y^{\text{rot}}, (q_x^{\text{rot}})^{-1}) \\ \arctan(q_z^{\text{rot}} (\sqrt{q_x^{\text{rot}2} + q_y^{\text{rot}2})^{-1}) \end{bmatrix}, \quad (22)$$

where  $Q_{d,\theta,\phi}^{\text{rot}} = [d_{kl}^{\text{rot}}, \theta_{kl}^{\text{rot}}, \phi_{kl}^{\text{rot}}]$ . It is important to note that HMD rotation affects only the HMD's orientation relative to the AP ( $\theta_{kl}$  and  $\phi_{kl}$ ) without altering the HMD-AP distance ( $d_{kl}$ ), assuming the distance between the head center and VR antennas is negligible compared to the head-to-AP distance, as illustrated in Fig. 4(b).

Denoting  $Q_{d,\theta,\phi}^0 = [d^0, \theta^0, \phi^0]$  as the initial orientation vector, the misalignment orientation vector due to combined

translation and rotation movements with respect to the initial orientation is formulated as:

$$Q_{d,\theta,\phi}^{\text{mis}} = 2Q_{d,\theta,\phi}^0 - (Q_{d,\theta,\phi}^{\text{trn}} + Q_{d,\theta,\phi}^{\text{rot}}). \quad (23)$$

$Q_{d,\theta,\phi}^{\text{mis}} = [d^{\text{dis}}, \theta^{\text{mis}}, \phi^{\text{mis}}]$ , where  $d^{\text{dis}}$  represents the HMD-AP distance discrepancy due to displacement,  $\theta^{\text{mis}}$  and  $\phi^{\text{mis}}$  denote the misalignment in the azimuth and elevation directions, respectively.

#### IV. PREDICTIVE BEAM TRANSITION

As an alternative to IMU-based tracking, an IMU-free beam tracking approach should also be considered, as varying IMU sampling rates vary across devices hinder standardising the beam re-alignment period. Additionally, delays in IMU data delivery to the beamformer can result in late beam transitions. IMU-free beam prediction methods address these challenges by enabling real-time beam adjustments without reliance on external motion sensors.

To ensure a smooth beam transition during HMD movement, which is primarily caused by head rotation, the HMD must preemptively predict the next best beam to switch to in order to maintain reception gain. The beam transition can either be triggered by a drop in received signal strength (RSS) below a certain threshold, or executed periodically. An example of the latter approach is IEEE 802.11ad/ay, where periodic beam training occurs at each beacon interval [35], [36]. Nevertheless, both methods require an exhaustive scan of the entire beam codebook to re-align both the Tx and Rx beams whenever a misalignment occurs.

The work in [28] implements beam tracking based on the best beam selection from neighbouring beams by observing the EVM parameter. It suggests using a small grid spacing of  $1^\circ$  &  $3^\circ$  to maintain smooth transition performance. However, such a narrow beam spacing presents significant complexity for mmWave user devices, which typically have limited array sizes and beam codebooks. In addition, using fine-grained beam spacing increases the number of scans during initial beam training, which results in higher power consumption, a critical factor given the limited battery capacity of the HMD.

We propose a predictive beam transition method that mitigates the impact of beam transition during HMD movement, requiring a minimal number of scans. This method enables the HMD to detect the misalignment and determine the future beam to transition to, thereby minimising gain loss during the beam transition. The prediction algorithm relies on the RSS observation from neighbouring beams surrounding the communicating beam, without requiring input from the IMU sensor. We present two following methods for predicting the future beam:

- M1:** Utilising only the magnitude and trend of the received signal level from individual neighbouring beams;
- M2:** Considering both the magnitude and trend of the received signal level from individual neighbouring

TABLE 1. Individual beam assignment and neighbour-beam grouping.

Direction	Individual beam	Neighbour-beam group
Northwest	$\mathbf{b}_{NW} = \mathbf{b}_1$	$\mathbf{B}_{NW} = \{\mathbf{b}_1, \mathbf{b}_2, \mathbf{b}_4\}$
North	$\mathbf{b}_N = \mathbf{b}_2$	$\mathbf{B}_N = \{\mathbf{b}_1, \mathbf{b}_2, \mathbf{b}_3\}$
Northeast	$\mathbf{b}_{NE} = \mathbf{b}_3$	$\mathbf{B}_{NE} = \{\mathbf{b}_2, \mathbf{b}_3, \mathbf{b}_5\}$
West	$\mathbf{b}_W = \mathbf{b}_4$	$\mathbf{B}_W = \{\mathbf{b}_1, \mathbf{b}_4, \mathbf{b}_6\}$
East	$\mathbf{b}_E = \mathbf{b}_5$	$\mathbf{B}_E = \{\mathbf{b}_3, \mathbf{b}_5, \mathbf{b}_8\}$
Southwest	$\mathbf{b}_{SW} = \mathbf{b}_6$	$\mathbf{B}_{SW} = \{\mathbf{b}_4, \mathbf{b}_6, \mathbf{b}_7\}$
South	$\mathbf{b}_S = \mathbf{b}_7$	$\mathbf{B}_S = \{\mathbf{b}_6, \mathbf{b}_7, \mathbf{b}_8\}$
Southeast	$\mathbf{b}_{SE} = \mathbf{b}_8$	$\mathbf{B}_{SE} = \{\mathbf{b}_5, \mathbf{b}_7, \mathbf{b}_8\}$

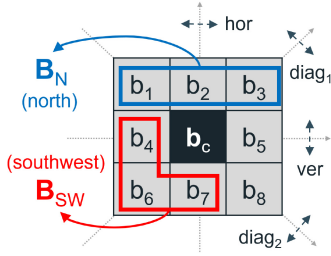


FIGURE 5. Neighbour-beam indexing, grouping, and transition direction.

beams, as well as the pairwise correlation within subsets of a beam group.

The magnitude and trend of the received signal level metrics in both methods provide insights into the relative strength of the beam and the signal variation trend during transitions, aiding in tracking the future beam candidate. Beam grouping in **M2** identifies the transition direction: horizontal, vertical or diagonal, enabling the selection of the optimal future beam, especially in scenarios involving diagonal transitions. In such cases, relying only on **M1** may result in suboptimal beam selection. The pseudocode for predictive beam transition using both methods is presented in Algorithm 1. A detailed explanation of individual neighbour-beam assignment and neighbour-beam grouping is provided in the following subsections.

#### A. INDIVIDUAL NEIGHBOUR-BEAM ASSIGNMENT

The first step comprises assigning each individual neighbouring beam to one of eight compass directions relative to the communication beam,  $\mathbf{b}_c$ . The assignment of the eight neighbouring beams,  $\mathbf{b}_{\text{neigh}}$ , is outlined in Table 1 and Fig. 5. The received signal level  $|y_{\mathbf{b}}|$  of all neighbouring beams at time instance  $t$  are denoted as:

$$Y(t) = \{|y_{NW}(t)|, |y_N(t)|, \dots, |y_S(t)|, |y_{SE}(t)|\}, \quad (24)$$

where  $Y(t) \in \mathbb{C}^{1 \times 8}$ . The fast beam steering and inter-beam switching time, typically on the order of tens of nanoseconds (ns) [37], is negligible compared to the interval period, which occurs every tens to hundred of milliseconds (ms). The normalised received signal level at time instance  $t$  is denoted as:

$$\bar{y}_{\mathbf{b}}(t) = \frac{|y_{\mathbf{b}}(t)|}{\max(Y(t))}. \quad (25)$$

#### Algorithm 1: Predictive Beam Transition **M1** and **M2**

---

**Input:**  $\mathbf{b}_c, Y(t)$   
**Output:**  $\mathbf{b}_f^{\mathbf{M1}}, \mathbf{b}_f^{\mathbf{M2}}$

- 1 Individual neighbour-beam assignment:  $\mathbf{b}_{\text{neigh}}$
- 2 Neighbour-beam grouping:  $\mathbf{B}_{\text{neigh}}$
- 3 **for**  $t \leq t_w$  **do**
- 4     **for each**  $\mathbf{b}_i \in \mathbf{b}_{\text{neigh}}$  **do**
- 5         Normalised Rx level:  $\bar{y}_{\mathbf{b}}(t)$  (25)
- 6         Normalised Rx level gradient:  $\bar{\nabla} y_{\mathbf{b}}(t)$  (28)
- 7         Prediction parameter **M1**:  $\mu_{\mathbf{b}}$  (29)
- 8         **for each**  $\mathbf{B}_i \in \mathbf{B}_{\text{neigh}}$  **do**
- 9             Beam group correlation:  $\bar{r}_{\mathbf{B}}(t)$  (31)
- 10             Prediction parameter **M2**:  $\rho_{\mathbf{b}}$  (32)
- 11         **for each**  $\mu_{\mathbf{b}} \in \mathcal{M}$  **do**
- 12             **if**  $\mu_{\mathbf{b}} \geq \mu_{\mathbf{b}}^{\text{th}}$  **then**
- 13                 Predicted future beam **M1**:  
                        $\mathbf{b}_f^{\mathbf{M1}} \leftarrow \arg \max(\mathcal{M})$
- 14                 Direction determination:  $\rho_{\text{dir}}$  (33)
- 15                 Direction discrepancy:  $\Delta\rho$  (34)
- 16                 **for each**  $\rho_{\text{dir}} \in \mathcal{P}_{\text{dir}}$  **do**
- 17                     **if**  $\rho_{\text{ver}} \geq \rho_{\text{dir}}^{\text{th}}$  or  $\rho_{\text{hor}} \geq \rho_{\text{dir}}^{\text{th}}$  **then**
- 18                         **if**  $\Delta\rho \geq \Delta\rho^{\text{th}}$  **then**
- 19                             Predicted future beam **M2**:  
                            $\mathbf{b}_f^{\mathbf{M2}} \leftarrow \arg \max(\mathcal{P}_{\text{hor}} \text{ or } \mathcal{P}_{\text{ver}})$
- 20                         **else**
- 21                             Predicted future beam **M2**:  
                            $\mathbf{b}_f^{\mathbf{M2}} \leftarrow \arg \max(\mathcal{P}_{\text{diag}_1} \text{ or } \mathcal{P}_{\text{diag}_2})$

---

Following that, the gradient of the received signal levels, indicating the trends in the received signal, is calculated for each neighbouring beam at each observation time as follows:

$$\nabla y_{\mathbf{b}}(t) = |y_{\mathbf{b}}(t)| - |y_{\mathbf{b}}(t-1)|. \quad (26)$$

The gradient matrix of all neighbouring beams is expressed as:

$$\nabla Y(t) = \{\nabla y_{NW}(t), \nabla y_N(t), \dots, \nabla y_S(t), \nabla y_{SE}(t)\}, \quad (27)$$

where  $\nabla Y(t) \in \mathbb{C}^{1 \times 8}$ . The normalised gradient at time instance  $t$  is denoted as:

$$\bar{\nabla} y_{\mathbf{b}}(t) = \frac{\nabla y_{\mathbf{b}}(t)}{\max(\nabla Y(t))}. \quad (28)$$

We define  $\mu_{\mathbf{b}}$  as the prediction parameter used in **M1**, which integrates both the received signal level and the gradient of each neighbouring beam within the observation window  $t_w$ , formulated as:

$$\mu_{\mathbf{b}} = \frac{1}{t_w} \sum_{t=1}^{t_w} \bar{y}_{\mathbf{b}}(t) \bar{\nabla} y_{\mathbf{b}}(t). \quad (29)$$

The **M1** prediction parameter of all beams are denoted as  $\mathcal{M} = \{\mu_{NW}, \mu_N, \dots, \mu_S, \mu_{SE}\}$ . Note that changes in the

channel gain (i.e., in case of a larger Tx–Rx distance), do not affect  $\mu_{\mathbf{b}}$ , since the received signal level is normalised at each observation time. The future beam  $\mathbf{b}_f$  is selected as the neighbouring beam with the highest  $\mu_{\mathbf{b}}$ .

### B. NEIGHBOUR-BEAM GROUPING

In the **M2** method, an additional step involving calculation of pairwise correlation within subsets of a beam group is required. Fig. 5 illustrates the neighbour-beam grouping,  $\mathbf{B}_{\text{neigh}}$ , based on compass direction. For example, the three beams located above the communication beam  $\mathbf{b}_c$  are grouped into the north-beam group, denoted as  $\mathbf{B}_N = \{\mathbf{b}_1, \mathbf{b}_2, \mathbf{b}_3\}$ . Table 1 details the beam grouping for all neighbouring beams of  $\mathbf{b}_c$ . This beam-grouping is crucial for identifying the misalignment direction, as the three beams within a group experience similar RSS trends upon misalignment, which enhances prediction accuracy. For instance, if the HMD rotates towards the upper-right direction, then the RSS of the three beams in southwest-beam group ( $\mathbf{B}_{\text{SW}}$ ) will increase, resulting in strong positive correlations within the  $\mathbf{B}_{\text{SW}}$  subset.

The correlation between received signal level of two beams,  $y_i$  and  $y_j$ , within a group is calculated as follows:

$$r_{y_i, y_j}(t) = \frac{\sum_{t=1}^{t_w} (|y_i(t)| - \bar{y}_i)(|y_j(t)| - \bar{y}_j)}{\sqrt{\sum_{t=1}^{t_w} (|y_i(t)| - \bar{y}_i)^2} \sqrt{\sum_{t=1}^{t_w} (|y_j(t)| - \bar{y}_j)^2}} \quad (30)$$

where  $\bar{y}_i$  and  $\bar{y}_j$  are the mean values of  $|y_i|$  and  $|y_j|$  over time instance  $t$  within the observation window of length  $t_w$ . Subsequently, the average correlation for beam group  $\mathbf{B}$  is calculated as follows:

$$\bar{r}_{\mathbf{B}}(t) = \frac{1}{3}(r_{y_i, y_j}(t) + r_{y_i, y_k}(t) + r_{y_j, y_k}(t)). \quad (31)$$

Nevertheless, the correlation coefficient alone is insufficient for accurate future beam prediction, as multiple beam groups may exhibit similarly strong correlations, particularly during diagonal transitions. To improve prediction accuracy, it is necessary to consider both the received signal level of each individual beam  $\bar{y}_{\mathbf{b}}(t)$  and its gradient  $\bar{\nabla}y_{\mathbf{b}}(t)$ , as calculated in (25) and (28), respectively.

We define  $\rho_{\mathbf{b}}$  as the prediction parameter used in **M2** to identify the transition direction. This parameter integrates the correlation, received signal level and gradient of each neighbouring beam within the observation window  $t_w$ , and is formulated as:

$$\rho_{\mathbf{b}} = \frac{1}{t_w} \sum_{t=1}^{t_w} \bar{r}_{\mathbf{B}}(t) \bar{y}_{\mathbf{b}}(t) \bar{\nabla}y_{\mathbf{b}}(t). \quad (32)$$

To determine the direction of the beam transition, as depicted in Fig. 5, the prediction parameters for two opposite directions, denoted as  $\rho_{\text{dir}}$ , are calculated as follows:

$$\begin{aligned} \rho_{\text{ver}} &= |\rho_N - \rho_S|, \\ \rho_{\text{hor}} &= |\rho_W - \rho_E|, \end{aligned}$$

$$\begin{aligned} \rho_{\text{diag}_1} &= |\rho_{\text{NW}} - \rho_{\text{SE}}|, \\ \rho_{\text{diag}_2} &= |\rho_{\text{NE}} - \rho_{\text{SW}}|. \end{aligned} \quad (33)$$

The transition detection in **M2** is triggered when  $\rho_{\text{dir}}$  for one of the directions exceeds a threshold  $\rho_{\text{dir}}^{\text{th}}$ . The set of detected direction is denoted as  $\mathcal{P}_{\text{dir}}$ , consisting of two neighbouring beams in the opposite directions (i.e.,  $\mathcal{P}_{\text{hor}} = \{\rho_W, \rho_E\}$ ). However, diagonal transition often result in high values of both  $\rho_{\text{hor}}(t)$  and  $\rho_{\text{diag}}(t)$ , leading to ambiguity in identifying the correct transition direction. To resolve this, we calculate the discrepancy between the two maximum  $\rho_{\text{dir}}$  values as follows:

$$\Delta\rho = |\max(\Delta\rho_{\text{ver}}, \Delta\rho_{\text{hor}}) - \max(\Delta\rho_{\text{diag}_1}, \Delta\rho_{\text{diag}_2})|. \quad (34)$$

This discrepancy is then compared with the threshold  $\Delta\rho^{\text{th}}$ , empirically determined from our measurements, to distinguish between horizontal and diagonal transitions. The future beam  $\mathbf{b}_f$  is then determined by selecting the beam with the highest  $\rho_{\mathbf{b}}$  corresponding to the detected transition direction.

For both **M1** and **M2** methods, once the future beam  $\mathbf{b}_f$  is determined, periodic Rx level observations are performed at each sampling interval exclusively on  $\mathbf{b}_f$ . This reduces the number of scans from the previously considered eight neighbouring beams to just a single candidate future beam. During this observation, the Rx level ratio between the future beam  $y_{\mathbf{b}_f}$  and the current communication beam  $y_{\mathbf{b}_c}$  is calculated as follows:

$$\Delta y(t) = \frac{|y_{\mathbf{b}_f}(t)|}{|y_{\mathbf{b}_c}(t)|}. \quad (35)$$

To prevent early or late transitions, beam transition is executed once  $\Delta y(t)$  reaches the threshold  $\Delta y^{\text{th}}$ .

## V. EXPERIMENTAL SETUP

We conducted experiments using our mmWave testbed, operating in the unlicensed 60 GHz band, to evaluate the performance of dual-connectivity in VR scenario and validate the proposed predictive beam transition approach.

### A. MMWAVE TESTBED

Our mmWave testbed comprises of two main components: a baseband module and an RF front-end module, as shown in Fig. 6(a). The baseband module is built on the AMD Xilinx Zynq UltraScale+ RFSoc ZCU111 [38], which integrates multiple analog-to-digital/digital-to-analog (AD/DA) converters capable of giga sample rates (up to 3.5 Gsps), meeting high throughput requirements in mmWave communication [39], [40]. The RF front-end module is built on Pharrowtech PTB1060 EVB [41]. The system operates in the unlicensed 60 GHz band (57 to 71 GHz) and features built-in up/down conversion. The control commands between RFSoc and PTB1060 are sent through the general-purpose input/output (GPIO) interfaces.

The Pharrowtech PTB1060 front-end platform comprises PTR1060 radio chip and PTM1060 antenna module, consisting of  $8 \times 8$  element-sized on-chip patch antenna array

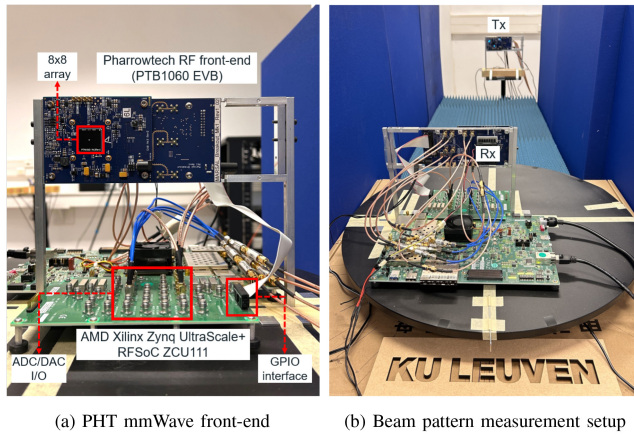


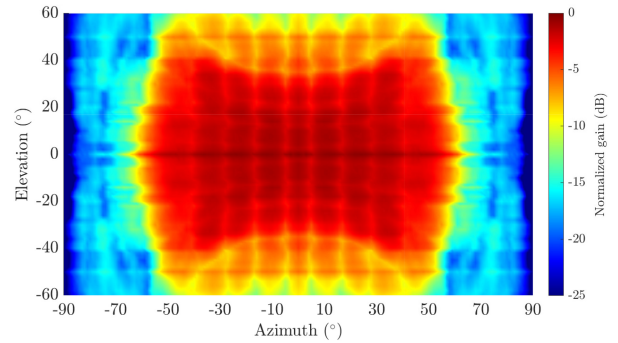
FIGURE 6. KU Leuven mmWave testbed.

for transmission or reception. The array has a physical dimension of  $20\text{ mm} \times 20\text{ mm}$  and is driven by 32 IOs of the radio-frequency integrated circuit (RFIC). The antenna element spacing in the azimuth plane is half-wavelength, while the spacing in the elevation plane is greater than half-wavelength, causing grating lobes in the elevation plane. The beam steering is enabled through 64 available beam codebook stored in the RFSoc platform. The codebook includes one quasi-omni beam steered at broadside and 63 directional beams, which are steered at combinations of nine azimuth angles,  $\theta_{BC} = \{0^\circ, \pm 12^\circ, \pm 24^\circ, \pm 36^\circ, \pm 48^\circ\}$ , and seven elevation angles,  $\phi_{BC} = \{0^\circ, \pm 9^\circ, \pm 18^\circ, \pm 27^\circ\}$ .

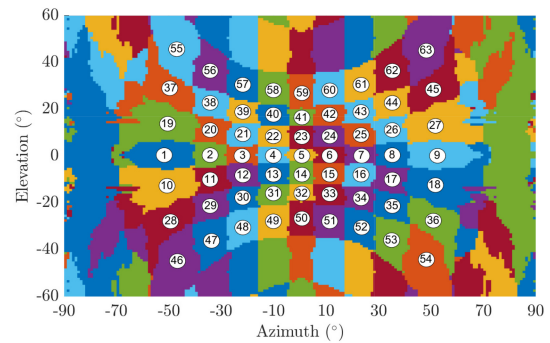
### B. BEAM PATTERN MEASUREMENT

We measure the beam pattern of all available beams in the codebook. The measurement setup is shown in Fig. 6(b). The Tx front-end is fixed in position, while the Rx front-end is mounted on a rotating platform, with the array centered at the axis of rotation. The rotating platform enables  $360^\circ$  rotation in the azimuth plane with  $0.5^\circ$  resolution. The Tx front-end transmits a sine-waveform through the broadside beam (beam index 5), while the Rx front-end switches all 64 beams to receive the signal. The received signal strength for each Rx beam is recorded every  $1^\circ$  rotation step. RF absorbers are placed around the Tx and Rx front-ends to attenuate reflections from the surrounding environment.

Fig. 7(a) shows the maximum radiation pattern of all beams. The  $9 \times 7$  directional beams provides up to  $\pm 60^\circ$  coverage in both azimuth and elevation directions. Strong grating lobes are observed in the elevation direction due to element spacing in that direction exceeding half a wavelength. Fig. 7(b) depicts the beam index of all  $9 \times 7$  directional beams projected on a 2D serving area at the measurement distance of 1.6 m, showing that the beams steered away from the broadside cover a relatively larger area compared to those close to the broadside. The azimuth half-power beamwidth (HPBW) ranges from  $\text{HPBW}_\theta \in [17^\circ, 25^\circ]$ , while the elevation HPBW ranges from  $\text{HPBW}_\phi \in [17^\circ, 28^\circ]$ .



(a) Maximum radiation pattern of all beams



(b) Beam index

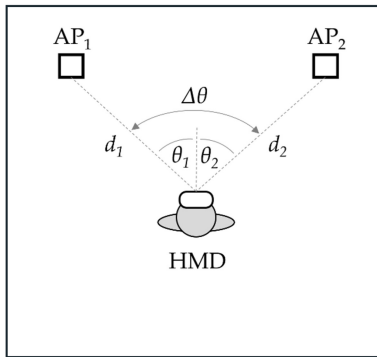
FIGURE 7. Measured beam patterns.

### C. DUAL-CONNECTIVITY VR MEASUREMENT

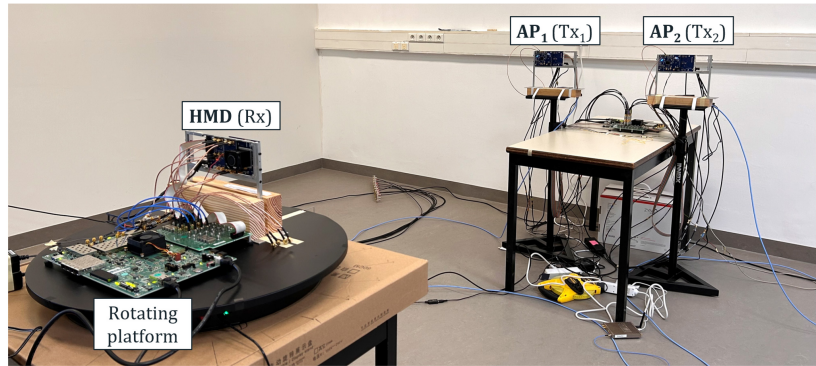
The measurements to evaluate the performance of dual-connectivity in a VR application were carried out in a  $7.4 \times 6.8\text{ m}^2$  lab environment. We consider a dual-AP scenario where two APs ( $\text{Tx}_1$  and  $\text{Tx}_2$ ) are spatially distributed to serve an HMD (Rx), as illustrated in Fig. 8. For comparison, a single-AP scenario is also deployed, with a pair of Tx and Rx placed facing each other's broadside. Both the AP(s) and HMD are mounted at a height of 1.2 m. In practical scenarios, APs are typically installed at a higher altitude than the HMD. However, due to the limitations of our testbed, specifically the GPIO cable length restricting the AP separation, we set the same height for both the AP(s) and the HMD. Furthermore, the investigation emphasises the HMD rotation in the azimuth plane, as it corresponds to yaw head motions that significantly impact AP(s)–HMD alignment.

In the dual-AP scenario, the HMD is positioned equidistantly between the two APs, resulting in identical distances ( $d_1 = d_2$ ) and symmetric azimuth orientations ( $|\theta_1| = |\theta_2|$ ) relative to each AP. The separation angle between two APs is denoted by  $\Delta\theta$ . We choose two separation angles ( $\Delta\theta = 24^\circ$  and  $96^\circ$ ) to investigate the impact of AP separation on signal reception performance, while maintaining the HMD–AP distances constant at  $d_1 = d_2 = 2.5\text{ m}$  for both separation angles.

On the AP side, the maximum length of the GPIO cable connecting the RFSoc board to each Tx front-end is 1.9 m, limiting the maximum spatial separation between the two

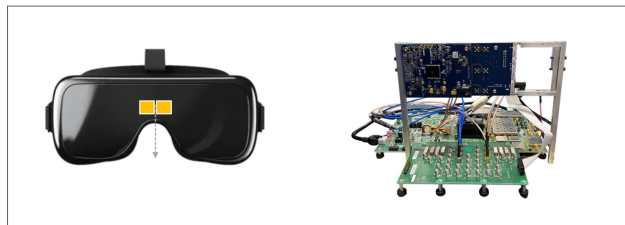


(a) Dual-connectivity VR setup

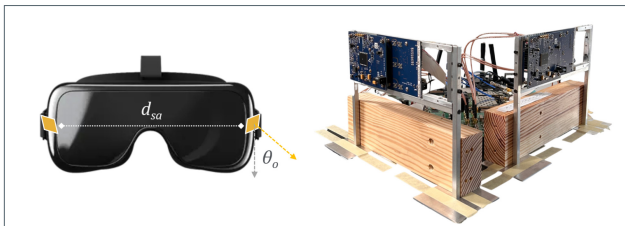


(b) Measurement layout

FIGURE 8. Dual-AP measurement setup.



(a) Co-located subarray



(b) Locally distributed subarray

FIGURE 9. Subarray configuration at the HMD.

APs to approximately 3.8 m. On the HMD side, the RFSoc board and Rx front-end(s) are mounted atop the rotating platform, with the array positioned about  $\sim 12$  cm from the rotation axis. Although the rotation platform supports  $360^\circ$  rotation in the azimuth direction, we limit rotation to  $\pm 150^\circ$  due to cabling flexibility limitation.

For the dual-connectivity scenario, we consider two subarray configurations at the HMD: co-located and locally distributed, as depicted in Fig. 9. In the co-located subarray configuration, two subarray units, each sized  $8 \times 8$ , are placed adjacent to each other at the center of the HMD, as shown in Fig. 9(a). However, due to physical constraints in our setup, we cannot place two front-end units side by side. Instead, we use a single front-end unit to act as two RxS by sequentially steering its Rx beams towards the two Tx directions.

In the locally distributed subarray configuration, each subarray is placed at the corner of the HMD with a broadside angle  $\theta_0$  and a subarray separation distance  $d_{sa}$ .

We employ two Rx front-end units placed perpendicularly, with  $\theta_0 = \pm 45^\circ$  and  $d_{sa} = 30$  cm, as shown in Fig. 9(b). This configuration aims to expand the HMD's FoV, which is particularly useful when the separation between APs is large.

For all measurement scenarios, including different separation distances from the AP and subarray HMD configurations, we capture complex channel information at each  $1^\circ$  rotation step from  $-150^\circ$  to  $+150^\circ$ . Before each channel capture, a beam alignment process is executed. We implement a beam training mechanism based on the transmit sector sweep (TxSS) and receive sector sweep (RxSS) procedures specified in the IEEE 802.11ad standard [35], which allows alignment between Tx and Rx beams. In the TxSS phase, the Tx sweeps through its available beams, sending a sine waveform while the receiver uses a quasi-omnidirectional beam pattern to receive the signal. The Rx records the signal strength for each Tx beam, with the strongest signal indicating the best Tx beam. Subsequently, we apply RxSS for Rx beam training, where the Tx transmits using the selected beam from TxSS, and the Rx sweeps its beams to measure the signal strength, identifying the best Rx beam for alignment.

#### D. BEAM TRANSITION MEASUREMENT

The measurements to validate the proposed predictive beam transition algorithm were conducted using a pair of mmWave Tx and Rx, similar to the beam pattern measurement setup shown in Fig. 6(b). Three beam transition directions: horizontal, vertical, and diagonal, were evaluated by mounting the Rx front-end in the corresponding orientations on a rotating platform, facing the Tx front-end, which was positioned in the horizontal orientation. The Rx array was positioned at the centre of rotating platform, rotating in  $0.5^\circ$  steps. At each step, the Rx levels of the communication beam and its eight neighbouring beams were recorded. We focus only on transitions between beams with eight neighbouring beams, excluding the edge beams from consideration.

## VI. RESULTS AND ANALYSIS

### A. EMULATION USING HMD MOVEMENTS DATASET

We used the 360° HMD movement datasets provided in [15] and [6] to emulate the HMD movement over time. Both datasets contain the 6DoF movement data of HMDs, collected from participants engaged in different video themes and games.

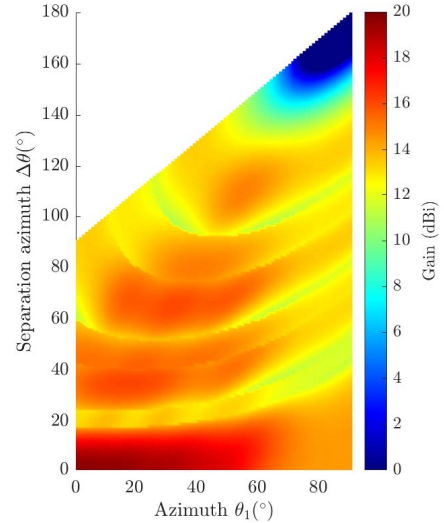
The first dataset, provided by [15], contains 6DoF movement data from participants watching ten different 360° video themes, including coaster, diving, sport and landscape. This dataset is characterised by relatively low translational movements, with dominant 360° head rotations. The 6DoF movement data is sampled every 40 ms using Oculus Rift DK2 HMD [42]. For our simulation, we selected all ten video themes collected from three participants.

The second dataset, collected by [6], provides the 6DoF movement data from participants playing three action games: Half-Life, Wrench, and Pistol Whip. This dataset is characterised by more frequent and rapid translational and rotational movements. The movement is sampled every 4 ms using HTC Vive Pro 2 HMD [43]. We selected data from all three games, each collected from seven participants.

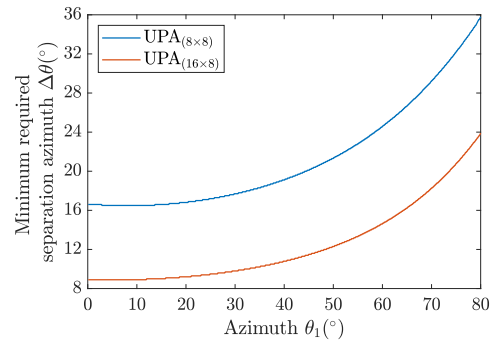
For each dataset, we limit the observation duration to 400 s and downsample the 6DoF data at 200 ms interval, assuming that the beam alignment process between the APs and HMD is completed within each interval. Using this movement data, we transform the HMD's physical movement into beam misalignment and simulate the mmWave communication channel between the APs and the HMD over time. This allows us to model the impact of HMD movement on time-varying signal reception caused by beam misalignment in a dynamic environment.

In our simulation, we model an indoor VR room with dimensions of  $20 \times 20 \text{ m}^2$ . Two APs are deployed symmetrically at a height of 4 m on one side of the room. For the initial observation point, an HMD with a height of 1.5 m is positioned around the center of a room. This results in equal distances ( $d_1 = d_2$ ) and identical azimuth angles ( $\theta_1 = \theta_2$ ) between the HMD and the two APs, as illustrated in Fig. 8(a). The separation angle between the two APs is denoted as  $\Delta\theta$ . We maintain the same HMD–AP distances,  $d_1 = d_2 = 10 \text{ m}$ , at the initial alignment and vary  $\Delta\theta$  to analyse the impact of AP separation on signal reception performance. This initial setup represents a typical VR scenario, where the user is positioned within the coverage area of the serving APs. The displacement and misalignment of the HMD occur over time, following the 6DoF movement data from the dataset.

Each AP transmits signals using a carrier frequency of 60 GHz with a bandwidth of 1.76 GHz. The transmit power is set at 10 dBm, and the HMD has a noise figure of 7 dB. We employ UPA<sub>(8×8)</sub> on both the HMD and AP sides, allowing both to steer their beams in the azimuth and elevation planes according to the HMD's position and orientation. Each AP generates a single transmit beam



(a) The beamforming gain of dual-beam



(b) The peak splitting point of dual-beam

**FIGURE 10.** The beamforming gain and peak splitting point of analog dual-beam over separation azimuth angles with  $\phi_1 = \phi_2 = 0^\circ$ ,  $\eta = 0.5$  and  $\theta_2 = \theta_1 - \Delta\theta$ .

directed at the HMD, while the HMD employs dual-beam reception as defined in (7).

As a baseline, we evaluated scenarios where the HMD utilises single-beam reception using a single RF chain and an array, served by a single AP. We also consider quasi-omni reception at the HMD, enabling it to receive transmissions from either a single AP or two APs. The quasi-omni beam is generated using a smaller array size, UPA<sub>(2×2)</sub>, generating a wider Rx beam in the azimuth and elevation directions. In this case, a fixed quasi-omni beam direction at  $(\theta_b, \phi_b) = (0^\circ, 0^\circ)$  is considered. Additionally, we consider hybrid beamforming to enable dual-beam reception at the HMD. Specifically, two RF chains control two subarrays, each beamforming towards a serving AP. For fair comparison, we maintain a total of 64 antenna elements, configured as two subarrays of UPA<sub>(8×4)</sub>.

### B. ANALOG DUAL-BEAMFORMING GAIN ANALYSIS

We evaluate the beamforming gain of two steered beams as function of the azimuth angle separation  $\Delta\theta$ , as presented in

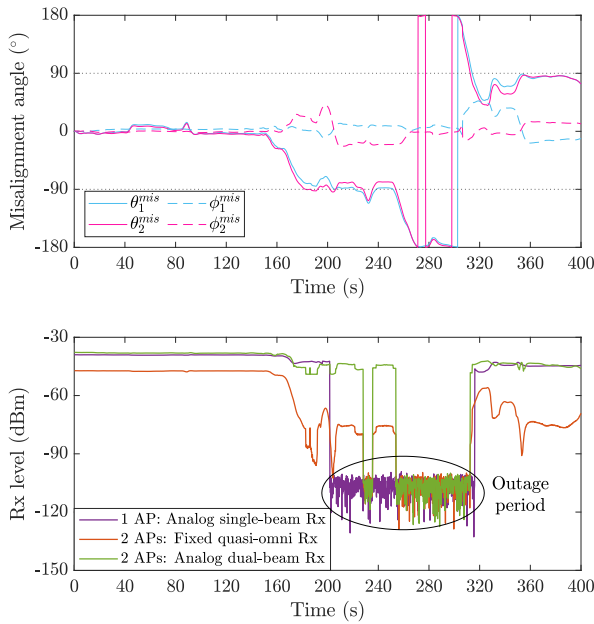


FIGURE 11. The impact of misalignment on the Rx level.

Fig. 10(a). The azimuth angle of the first beam is denoted as  $\theta_1$ , and the azimuth angle of the second beam is given by  $\theta_2 = \theta_1 - \Delta\theta$ . The elevation angle of both beams are set to  $\phi_1 = \phi_2 = 0^\circ$ . With equal power distribution between the two beams ( $\eta_1 = \eta_2 = 0.5$ ), the beamforming gains are identical in both steering directions,  $g(\theta_1, \phi_1) = g(\theta_2, \phi_2)$ . It shows that the maximum gain is achieved at  $\theta_1 = 0^\circ$  and  $\Delta\theta = 0^\circ$ , corresponding to a single beam steered at the azimuth angle of  $0^\circ$ . When the beam is split into two, the beamforming gain achieved in each intended direction decreases. Nevertheless, the gain reduction follows a non-linear relationship with increasing  $\Delta\theta$ , given in a fixed  $\theta_1$ . This is due to destructive interference occurring at certain angle combinations, as observed in Fig. 10(a). A significant gain reduction is noted when both beams are oriented away from the broadside and separated by a large  $\Delta\theta$ .

Fig. 10(b) depicts the splitting point of the dual-beam configuration, defined as the minimum separation angle  $\Delta\theta$  between two beams at which two distinct peaks are generated. Below this  $\Delta\theta$ , the beam exhibits only a single peak. The analysis focuses on the azimuth plane with  $\phi_1 = \phi_2 = 0^\circ$  and equal power distribution between the two beams ( $\eta_1 = \eta_2 = 0.5$ ). The evaluation considers two array sizes:  $UPA_{(8 \times 8)}$  and  $UPA_{(16 \times 8)}$ . Both array sizes exhibit similar trends, where an increase in the azimuth angle  $\theta_1$  requires a larger  $\Delta\theta$  for splitting. Increasing the array size, particularly in the azimuth plane, reduces the minimum  $\Delta\theta$  required due to the narrower beamwidth associated with larger arrays.

### C. DUAL-BEAM RECEPTION ANALYSIS

Fig. 11 shows the impact of HMD movement on the Rx signal level, evaluated from one sample from the datasets. The top subfigure illustrates the misalignment angle in the

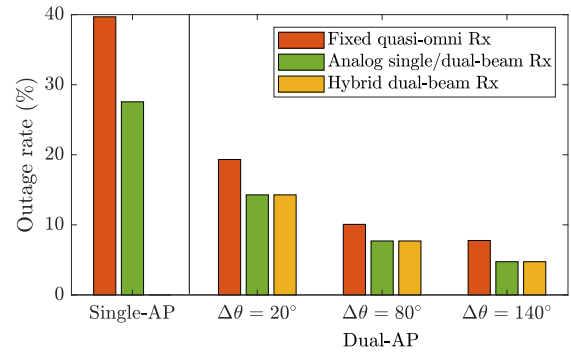


FIGURE 12. Simulated outage rate due to HMD movement.

azimuth and elevation planes, denoted as  $\theta^{\text{mis}}$  and  $\phi^{\text{mis}}$ , relative to the initial orientation between HMD and serving APs, evaluated over a 400 s period. The most significant misalignment occurs in the azimuth direction, primarily due to yaw head rotation. The discrepancy between  $\theta_1^{\text{mis}}$  and  $\theta_2^{\text{mis}}$  at each time step arises from the separation angle between the two APs.

The lower subfigure of Fig. 11 describes the Rx level resulting from the movement of HMD for various beam steering methods. Reception using a fixed quasi-omni pattern yields significantly lower and more fluctuating Rx levels compared to steered beams, even when the HMD is served by two APs. With periodic beam re-alignment in the steered single-beam and dual-beam cases, the Rx level is maintained as long as the serving AP remains within the HMD's FoV. Outages occur when the HMD rotates beyond  $\pm 90^\circ$  from an AP, as mmWave signals cannot diffract around the head sufficiently to contribute to the Rx level. The signal recovers once the AP re-enters the FoV. Relying on only one AP leads to outages occurring shortly after it exits the HMD's FoV. By distributing more APs, the outage period can be reduced, as one AP can remain serving the HMD for a longer duration.

We evaluated the impact of AP separation on the outage rate, defined as the total duration of outages divided by the total observation period. Fig. 12 shows the outage rate for various azimuth separations,  $\Delta\theta$ . A beamformed reception reduces the outage rate in all scenarios, significantly observed in the single-AP case. In the dual-AP scenario, the proposed analog dual-beam reception reduces the outage rate by 2.4%–5% compared to fixed quasi-omni reception. Larger AP separation further lowers the outage rate, achieving up to 22.8% improvement over single-beam reception, as it ensures the HMD remains covered by at least one AP for most of its rotation. Notably, our proposed analog dual-beam reception approach matches the outage performance of hybrid dual-beam reception, despite using only a single RF chain, highlighting its effectiveness in reducing outages.

We also assess the Rx signal level at the HMD during aligned (non-outage) periods. The violin plots in Fig. 13 show the distribution of Rx signal levels for various AP separation angles. At smaller azimuth separations ( $\Delta\theta = 20^\circ$ ), an average Rx level improvement is observed compared

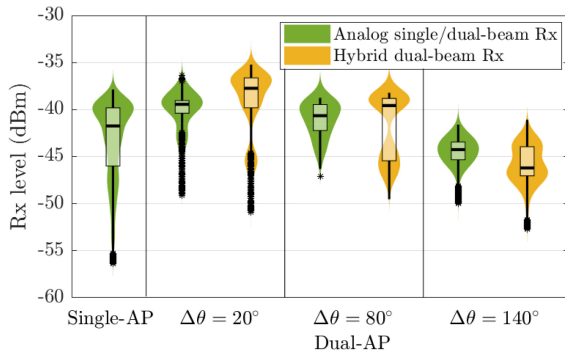


**FIGURE 13.** Simulated Rx level distribution of the steered single/dual beam Rx during the aligned (non-outage) period.

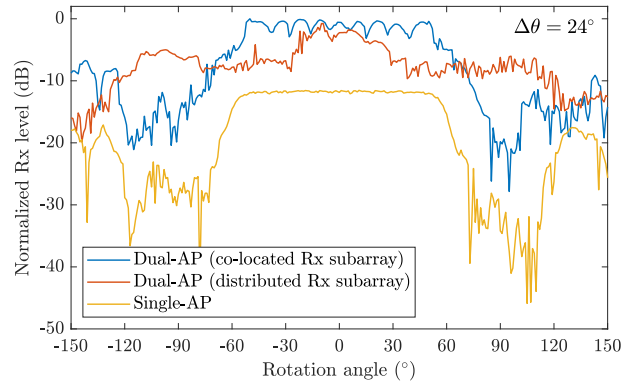
to the single-beam case, demonstrating the advantage of dual-beam reception. Hybrid dual-beam reception balances flexibility in single-beam steering per subarray with constraints from subarray size, resulting in a mix of strong and weak receptions. In contrast, the proposed analog dual-beam reception exhibits a less distributed Rx level, ensuring more stable reception essential for VR applications.

As the separation angle increases, the Rx level performance during aligned periods diminishes. At  $\Delta\theta = 140^\circ$ , the Rx level performance during aligned periods is no longer superior to the single-beam scenario. This degradation is primarily attributed to the reduced beamforming gain when steering multi-beams away from the broadside. Therefore, there is a trade-off between the robustness of widely separated APs in minimising outage rates and the Rx signal level experienced during aligned periods. These insights are crucial for planning AP deployment and designing AP selection strategies in mmWave CoMP networks serving the HMD with dual-beam reception capability.

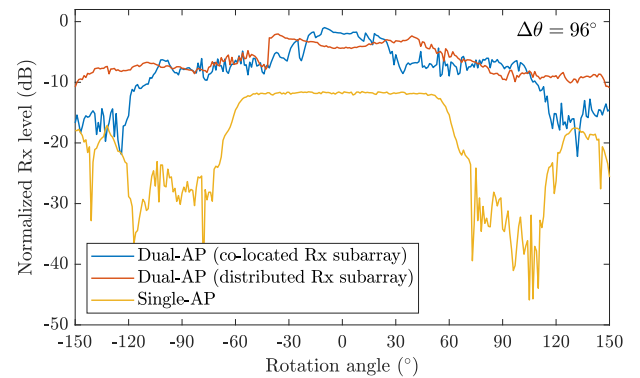
#### D. DUAL-CONNECTIVITY VR: EXPERIMENTAL ANALYSIS

We compare the Rx level during rotation for all scenarios, categorised by the number of APs (single or dual), the APs' separation angle, and the HMD's subarray configuration. Fig. 14(a) and Fig. 14(b) present the normalised Rx level for the evaluated AP and HMD configurations at AP separation angles of  $\Delta\theta = 24^\circ$  and  $\Delta\theta = 96^\circ$ , respectively. As a baseline, we conducted a measurement with single-AP scenario, which provides stable reception within the HMD's FoV spanning from  $-60^\circ$  to  $+60^\circ$ .

In the scenario with a small AP separation ( $\Delta\theta = 24^\circ$ ), the co-located Rx subarray configuration performs better than the distributed Rx subarray, particularly within the rotation angle range of  $[-60^\circ, +60^\circ]$ , as shown in Fig. 14(a). In this region, the HMD is effectively served by both APs. Beyond this range, the Rx level gradually decreases as the HMD rotates away from the serving APs. The distributed Rx subarray configuration, each facing towards  $+45^\circ$  and  $-45^\circ$  in the azimuth direction, expands the HMD's FoV, maintaining stable Rx levels within  $[-120^\circ, +120^\circ]$ . However, this configuration comes at the cost that the



(a) AP's separation angle  $\Delta\theta = 24^\circ$



(b) AP's separation angle  $\Delta\theta = 96^\circ$

**FIGURE 14.** Measured Rx level performance during rotation.

HMD is effectively served by both APs only within the  $[-30^\circ, +30^\circ]$  region.

Deploying the two APs with a larger separation angle ( $\Delta\theta = 96^\circ$ ) provides wider angular coverage. This separation enables the HMD with a co-located Rx subarray to maintain reception within  $[-120^\circ, +120^\circ]$ , at the cost of reducing the effective area served simultaneously by both APs, as shown in Fig. 14(b). At this separation angle, employing a distributed Rx subarray configuration at the HMD is advantageous, as it improves angular coverage within  $[-150^\circ, +150^\circ]$  and allows a larger area to be served simultaneously by both APs, compared to the co-located Rx subarray.

The violin plots presented in Fig. 15 show the distribution of the Rx level in various configurations. Compared to the single-AP scenario, the dual-AP deployment offers significant advantages in achieving higher Rx levels and broader angular coverage to cope with rapid head movements. The deployment of dual APs improves both the average and lower-bound Rx levels compared to the single-AP case. Increasing the separation angle from  $24^\circ$  to  $96^\circ$  enhances the lower-bound Rx level by up to 8.97 dB. In addition, implementing a distributed subarray improves the

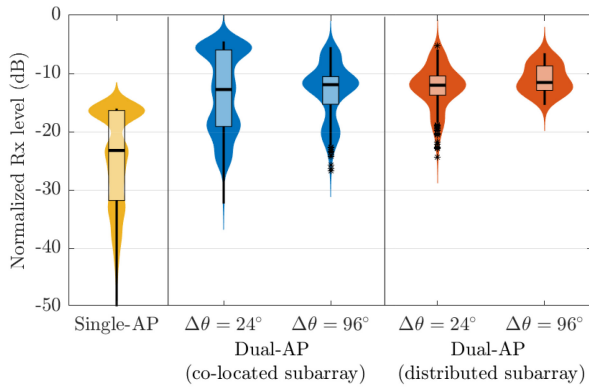


FIGURE 15. Measured Rx level distribution during rotation.

lower-bound Rx levels even further, with gains of up to 11.3 dB. The combination of a large AP separation and a distributed Rx subarray at HMD not only expands the FoV but also enhances the effective area covered by both APs simultaneously, providing more stable Rx level distribution during HMD movements.

### E. BEAM PREDICTION EVALUATION

The objective of our predictive beam transition mechanism is to identify the future beam to transition to upon misalignment and determine how early the HMD can predict this transition. By using the **M2** method, the transition direction is indicated by a high correlation ( $r$ ) between the beams within one or more neighbouring-beam groups. Fig. 16 depicts the pairwise correlation coefficient map between neighbouring beams. During horizontal transition, strong correlation coefficients are observed in either the  $\mathbf{B}_W$  or  $\mathbf{B}_E$  groups. For instance, Fig. 16(a) shows horizontal transition in the east direction, leading to strong correlation among beams in  $\mathbf{B}_E = \{r_{3,5}, r_{3,8}, r_{5,8}\}$ , highlighted by the red square. Fig. 16(b) presents the correlation during a vertical transition in the south direction, where strong correlations are observed among two opposite beam groups,  $\mathbf{B}_N$  and  $\mathbf{B}_S$ . These example emphasises that correlation  $r(t)$  alone is insufficient to predict the future beam. Other parameters, such as the Rx level  $y(t)$  and the Rx level gradient  $\nabla y(t)$ , also play important roles in determining the future beam, as outlined in (32).

For diagonal transitions, strong correlation coefficients are typically observed in both diagonal and horizontal directions. Fig. 16(c) shows an example of the correlation map during diagonal transition in the northwest direction, showing strong correlations in both the  $\mathbf{B}_{NW}$  and  $\mathbf{B}_W$  groups, highlighted by red and blue rectangles, respectively. Similarly, Fig. 16(d) shows the correlation among beams during a beam transition in the southwest direction, where the  $\mathbf{B}_{SW}$  and  $\mathbf{B}_W$  groups exhibit strong correlations. This behaviour is attributed to the similarity in the increasing trends of the received signal level in both directions, making it a unique characteristic for identifying transitions in the diagonal direction.

TABLE 2. Future beam prediction.

Method	Avg. pred. time (ms)		
	Horizontal	Vertical	Diagonal
Predictive <b>M1</b>	122	120	185
Predictive <b>M2</b>	146	132	227

The thresholds  $\rho_{dir}^{th}$  and  $\Delta\rho^{th}$  are set to trigger detection and differentiate between diagonal and horizontal/vertical directions. This distinction is based on the fact that either  $\Delta\rho_{ver}$  or  $\Delta\rho_{hor}$  is always greater than  $\Delta\rho_{diag}$ , even during diagonal transitions. The values  $\rho_{dir}^{th} = 0.5$  and  $\Delta\rho^{th} = 0.4$  are selected based on empirical measurement data across all transitions. The observation window  $t_w$  is set to four times the sampling period, and  $\Delta y_{th} = 0.95$  is chosen to prevent early transitions.

The future beam prediction time is defined as the time interval before the transition, during which the HMD detects movement and determines the appropriate neighbouring beam to switch to. Assuming a HPBW of  $15^\circ$  and a constant head rotation speed of  $300^\circ/s$ , the  $0.5^\circ$  rotation step corresponds to a 25 ms sampling period. Table 2 presents the average prediction time for both **M1** and **M2** methods, with **M2** providing 12–42 ms earlier prediction than **M1** across all transition directions. Early knowledge of the future beam,  $\mathbf{b}_f$ , reduces the number of scan required before beam switching, as the observation focuses only on  $\mathbf{b}_f$  rather than all eight neighbouring beams. Moreover, in both methods, diagonal transitions exhibit significantly longer prediction time compared to horizontal and vertical transitions, owing to the wider transition angle in the diagonal direction.

### F. BEAM TRANSITION PERFORMANCE

A smooth beam transition during user movement is important to minimise Rx level degradation, making the transition timing critical. Performing the transition either too early or too late can result in Rx level deterioration. We compare the performance of our predictive beam transition approach with two baseline methods: the 3-dB threshold method and the IEEE 802.11ad/ay standard. The first method adopts a reactive approach, triggering a beam transition only after detecting a 3-dB drop in the Rx level. Once triggered, an exhaustive search is conducted to re-align the Rx beam with the Tx beam. On the other hand, IEEE 802.11ad/ay standard employs a periodic beam re-alignment based on its beacon interval  $t_b$ , which ranges from 100 ms to 1 s [2]. During each  $t_b$ , an exhaustive search is carried out to identify the best Tx–Rx beam alignment.

Fig. 17 compares the beam transition performance of our proposed predictive approach with baseline methods. The 3-dB threshold method initiates transitions only after a 3-dB drop in Rx level, resulting in significant Rx level drop and instability during transitions. The IEEE 802.11ad/ay standard with  $t_b = 100$  ms improves transition performance, but late transitions are still frequently observed, as shown in Fig. 17(a). In contrast, our proposed predictive approach

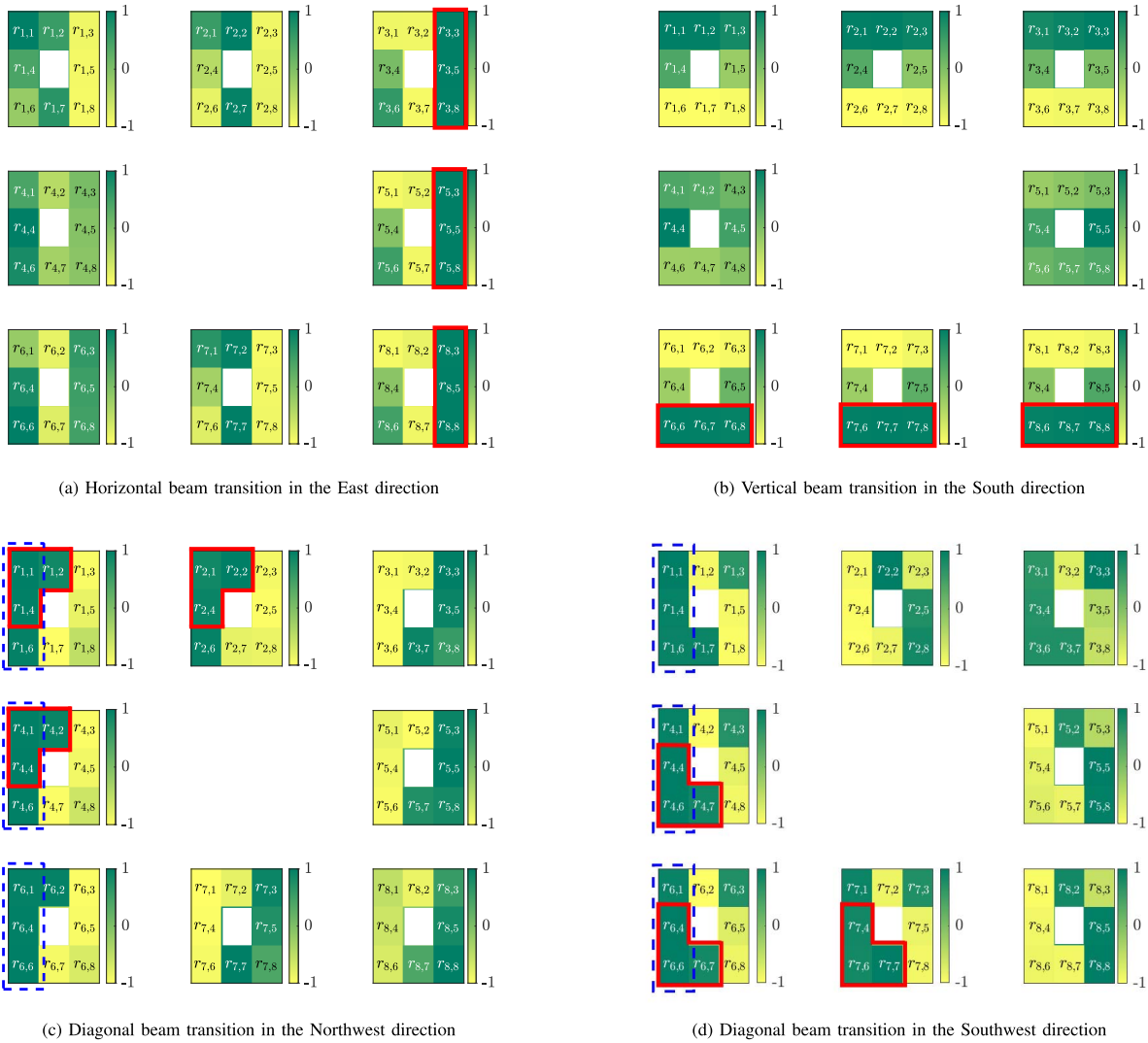


**FIGURE 16.** Pairwise correlation  $r$  map among sub-beams within beam groups. The red solid rectangle highlights strong correlation among three sub-beams corresponding to the transition direction. The blue dashed rectangle in (c) and (d) indicates strong correlation within another beam group, observed during diagonal transitions.

**TABLE 3.** Minimum Rx level during transition.

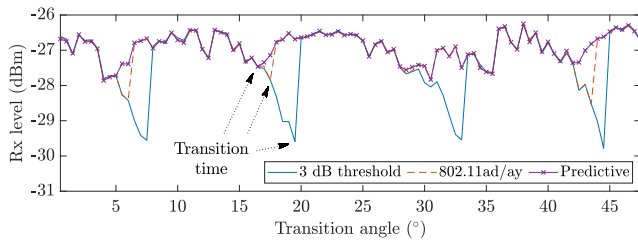
Method	Min. Rx level (dBm)		
	Horizontal	Vertical	Diagonal
3-dB threshold	-34.71	-38.17	-33.99
802.11ad/ay ( $t_b = 100$ ms)	-29.85	-35.47	-30.83
802.11ad/ay ( $t_b = 200$ ms)	-32.03	-35.74	-32.64
Predictive <b>M1</b>	-29.38	-35.47	-30.90
Predictive <b>M2</b>	-29.38	-35.47	-30.26

ensures timely transitions. The Rx level ratio, defined in (35) with  $\Delta_{y_{th}} = 0.95$ , prevents early transitions, while the 25 ms sampling period mitigates late beam transitions, thereby minimising Rx level drops during the transition process.

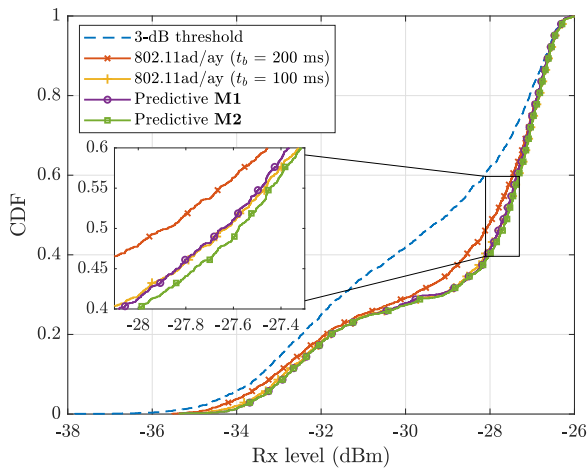
Fig. 17(b) and Table 3 present the Cumulative Distribution Function (CDF) and the minimum Rx level during beam transitions for all compared methods, respectively.

Both clearly demonstrate the superiority of the predictive **M2** approach over the other methods. Compared to the **M1** method, the predictive **M2** approach minimises the Rx level drop during diagonal transitions by leveraging the correlation coefficient for more accurate future beam prediction. In addition, the predictive **M1** and IEEE 802.11ad/ay methods with  $t_b = 100$  ms exhibit comparable performance. Doubling the beacon interval to  $t_b = 200$  ms in the IEEE 802.11ad/ay method significantly degrades the Rx level performance due to delayed beam transitions. For all methods, the low Rx level observed during vertical transitions, as shown in Table 3, results from misalignment between the Tx and Rx orientations in the measurement setup.

In addition to evaluating Rx level performance during transitions, we also evaluate the beam scanning overhead. Table 4 presents the number of required scans for each method during beam transitions. The scanning complexity of both the 3-dB threshold and IEEE 802.11ad/ay methods



(a) Rx level drop during transitions



(b) CDF of Rx level during beam transition

FIGURE 17. Beam transition performance.

is  $\mathcal{O}(N_{\text{exh}})$ , as both employ exhaustive scanning with  $N_{\text{exh}}$  beams to scan. With  $N_{\text{exh}} = 64$  beams, the 3-dB threshold method performs 64 scans whenever it detects a 3-dB Rx level drop. While effective for static applications, this reactive approach leads to significant Rx level degradation during transitions. For the IEEE 802.11ad/ay with  $t_b = 100$  ms, the overhead reaches 640 scans per second. Doubling the beacon interval halves the scanning overhead, demonstrating the trade-off between Rx level performance and scanning overhead. Meanwhile, our predictive approach requires a maximum of 360 scans per second, reducing the overhead by 43.8% compared to IEEE 802.11ad/ay with  $t_b = 100$  ms. This efficiency is achieved despite the shorter sampling interval of 25 ms, as only eight scans are performed per interval,  $\mathcal{O}(8)$ , covering the eight neighbouring beams. Once movement is detected and the future beam  $\mathbf{b}_f$  is determined, the scanning overhead is further reduced to just two scans per interval, focusing only on  $\mathbf{b}_c$  and  $\mathbf{b}_f$  until the transition is complete.

### G. PRACTICAL CONSIDERATION AND CHALLENGES

We have shown that multi-point connectivity can improve robustness against dynamic user movements in VR applications. While our study focuses on a single-user case, the multi-point connectivity networks can also support multiple HMDs. This requires APs to be equipped with multiple RF chains, enabling hybrid beamforming to serve multiple

TABLE 4. Scanning overhead.

Method	Complexity	Interval	No. of scans ( $N_{\text{exh}} = 64$ )
3-dB threshold	$\mathcal{O}(N_{\text{exh}})$	-	64 per trigger
802.11ad/ay	$\mathcal{O}(N_{\text{exh}})$	$t_b = 100$ ms	640 / s
		$t_b = 200$ ms	320 / s
Predictive	$\mathcal{O}(8)$	25 ms	up to 360 / s

users simultaneously. To mitigate inter-user interference, precoding techniques such as ZF or MMSE must be employed. Additionally, deploying more spatially distributed APs ensures  $360^\circ$  coverage and accommodates HMDs with various orientations.

At the HMD side, dual-beam reception, realised through either analog multi-beamforming or hybrid beamforming, can leverage the presence of multiple APs. This directive reception also reduces interferences compared to the omnireception. The challenge lies in the initial beam alignment with the candidate APs, where an exhaustive beam search may be required to find an optimal beam pair. In the analog multi-beamforming-based HMD, initial beam training must be executed sequentially for each serving AP, while in the hybrid-beamforming-based HMD, this can be done simultaneously. Furthermore, compressed sensing can be considered to accelerate the initial beam training. Once the beam pair is established, a lightweight beam tracking method should be employed to enable seamless transitions during movement.

The proposed IMU-free beam prediction improves efficiency by narrowing the beam search to just the eight neighboring beams around the current beam. This reduction in the search space makes the tracking process more lightweight and efficient. Additionally, the proposed prediction method maintains a constant computational cost per step, eliminating the need for costly state space estimation and correction typically required in the EKF or probabilistic tracking approach. Furthermore, we have demonstrated that the beam prediction approach works with mmWave devices using pre-defined beam codebooks.

The performance analysis of beam prediction focuses on single-beam tracking at the HMD. However, it can be extended to dual-beam tracking, particularly in configurations where two RF chains and arrays are used at the HMD. In such cases, the tracking is performed independently for each array, as the transition direction of one subarray is generally uncorrelated with that of the other. For example, if the user moves translationally to the right along the  $y$ -axis, both HMD beams may transition to the neighbouring beams in the west direction. Conversely, if the user moves closer to the APs along the  $x$ -axis, one beam might switch to the west neighbour while the other transitions to the east neighbour. Additionally, different rotational movements, such as yaw or roll, can lead to varying tracking outcomes, further emphasising the importance of independent beam tracking for each array.

## VII. CONCLUSION

This paper presents a user-movement-robust solution for mmWave-based VR applications by integrating mmWave coordinated dual-AP networks with steerable dual-beam reception at the HMD, mitigating outages caused by frequent user head movements. Simulation results, incorporating a beam misalignment model and real HMD movement datasets, demonstrate that the deployment of APs with large separation distances effectively reduces outage rates, albeit with the cost of reduced Rx levels during aligned periods. Experimental validation emphasises the benefits of combining large AP separation with a locally distributed Rx subarray at the HMD, enhancing angular coverage and alleviating the out-of-field-of-view impact caused by head rotation. Additionally, to achieve ideal beam tracking, this work proposes an efficient beam prediction method capable of predicting the next beam to transition to before an outage occurs. This method prevents Rx level degradation during beam transitions while significantly reducing scanning overhead by focusing only on neighbouring beams. Future work could explore optimising beam power distribution for analog multi-directional beamforming, expanding AP deployments to achieve 360° coverage, analysing the impact of blockage and interference in multi-user scenarios, and utilising analog multi-directional beamforming for beam tracking.

## REFERENCES

- [1] J. Struye, F. Lemic, and J. Famaey, "Towards ultra-low-latency mmWave Wi-Fi for multi-user interactive virtual reality," in *Proc. IEEE Glob. Commun. Conf. (GLOBECOM)*, 2020, pp. 1–6.
- [2] T. Nitsche, C. Cordeiro, A. B. Flores, E. W. Knightly, E. Perahia, and J. C. Widmer, "IEEE 802.11ad: Directional 60 GHz communication for multi-gigabit-per-second Wi-Fi [invited paper]," *IEEE Commun. Mag.*, vol. 52, no. 12, pp. 132–141, Dec. 2014.
- [3] Y. Ghasempour, C. R. Da Silva, C. Cordeiro, and E. W. Knightly, "IEEE 802.11ay: Next-generation 60 GHz communication for 100 Gb/s Wi-Fi," *IEEE Commun. Mag.*, vol. 55, no. 12, pp. 186–192, Dec. 2017.
- [4] (Extron, East Ball Road Anaheim, CA, USA). *8K Data Rate Calculator*. Accessed: Dec. 17, 2024. [Online]. Available: <https://www.extron.com/product/videtools.aspx>
- [5] J. Struye et al., "Opportunities and challenges for virtual reality streaming over Millimeter-wave: An experimental analysis," in *Proc. 13th Int. Conf. Netw. Future (NoF)*, 2022, pp. 1–5.
- [6] A. Marinšek, S. De Kunst, G. Callebaut, L. De Strycker, and L. Van der Perre, "mmWave for extended reality: Open user mobility Dataset, Characterization, and impact on link quality," *IEEE Commun. Mag.*, vol. 62, no. 8, pp. 24–30, Aug. 2024.
- [7] P. Yang, T. Q. S. Quek, J. Chen, C. You, and X. Cao, "Feeling of presence maximization: MmWave-enabled virtual reality meets deep reinforcement learning," *IEEE Trans. Wireless Commun.*, vol. 21, no. 11, pp. 10005–10019, Nov. 2022.
- [8] D. Maamari, N. Devroye, and D. Tuninetti, "Coverage in mmWave cellular networks with base station co-operation," *IEEE Trans. Wireless Commun.*, vol. 15, no. 4, pp. 2981–2994, Apr. 2016.
- [9] I. K. Jain, R. Subbaraman, and D. Bharadia, "Two beams are better than one: Towards reliable and high throughput mmWave links," in *Proc. ACM SIGCOMM Conf.*, 2021, pp. 488–502. [Online]. Available: <https://doi.org/10.1145/3452296.3472924>
- [10] N. Grosheva, R. Hersyandika, J. Widmer, and S. Pollin, "In-band multi-connectivity with local beamtraining for improving mmWave network resilience," in *Proc. Int'l ACM Conf. Model. Anal. Simul. Wireless Mobile Syst.*, 2023, pp. 277–284. [Online]. Available: <https://doi.org/10.1145/3616388.3617529>
- [11] S. Gupta, J. Chakareski, and P. Popovski, "Millimeter wave meets edge computing for mobile VR with high-fidelity 8K scalable 360° video," in *Proc. IEEE 21st Int. Workshop Multimedia Signal Process. (MMSP)*, 2019, pp. 1–6.
- [12] J. Chakareski, M. Khan, T. Ropitault, and S. Blandino, "Millimeter wave and free-space-optics for future dual-connectivity 6DOF mobile multi-user VR streaming," *ACM Trans. Multimedia Comput. Commun. Appl.*, vol. 19, no. 2, pp. 1–25, Feb. 2023. [Online]. Available: <https://doi.org/10.1145/3544494>
- [13] J. Bao, D. Sun, and H. Li, "Motion sensor aided beam tracking in mobile devices of Millimeter-wave communications," in *Proc. IEEE Int. Conf. Commun. (ICC)*, 2018, pp. 1–7.
- [14] Y. Lin, C. Shen, and Z. Zhong, "Sensor-aided predictive beam tracking for mmWave phased array antennas," in *Proc. IEEE Globecom Workshops (GC Wkshps)*, 2019, pp. 1–5.
- [15] W.-C. Lo, C.-L. Fan, J. Lee, C.-Y. Huang, K.-T. Chen, and C.-H. Hsu, "360° video viewing dataset in head-mounted virtual reality," in *Proc. 8th ACM Multimedia Syst. Conf.*, 2017, pp. 211–216. [Online]. Available: <https://doi.org/10.1145/3083187.3083219>
- [16] X. Corbillon, F. De Simone, and G. Simon, "360-degree video head movement dataset," in *Proc. 8th ACM Multimedia Syst. Conf.*, 2017, pp. 199–204. [Online]. Available: <https://doi.org/10.1145/3083187.3083215>
- [17] E. J. David, J. Gutiérrez, A. Coutrot, M. P. Da Silva, and P. L. Callet, "A dataset of head and eye movements for 360° videos," in *Proc. 9th ACM Multimedia Syst. Conf.*, 2018, pp. 432–437.
- [18] A. Alkhateeb, G. Leus, and R. W. Heath, "Compressed sensing based multi-user millimeter wave systems: How many measurements are needed?" in *Proc. IEEE Int. Conf. Acoust., Speech Signal Process. (ICASSP)*, 2015, pp. 2909–2913.
- [19] V. Va, J. Choi, T. Shimizu, G. Bansal, and R. W. Heath, "Inverse multipath fingerprinting for millimeter wave V2I beam alignment," *IEEE Trans. Veh. Technol.*, vol. 67, no. 5, pp. 4042–4058, May 2018.
- [20] T. Zhang, Y. Wang, M. Ouyang, L. Xing, and F. Gao, "Third-party camera aided beam alignment real-world prototype for mmWave communications," in *Proc. IEEE Wireless Commun. Netw. Conf. (WCNC)*, 2024, pp. 1–6.
- [21] M. Zecchin, M. B. Mashhadi, M. Jankowski, D. Gündüz, M. Kountouris, and D. Gesbert, "LIDAR and position-aided mmWave beam selection with non-local CNNs and curriculum training," *IEEE Trans. Veh. Technol.*, vol. 71, no. 3, pp. 2979–2990, Mar. 2022.
- [22] K. Vuckovic, M. B. Mashhadi, F. Hejazi, N. Rahnavard, and A. Alkhateeb, "PARAMOUNT: Toward Generalizable deep learning for mmWave beam selection using sub-6 GHz channel measurements," *IEEE Trans. Wireless Commun.*, vol. 23, no. 5, pp. 5187–5202, May 2024.
- [23] J. Struye, F. Lemic, and J. Famaey, "CoVRage: Millimeter-wave beamforming for mobile interactive virtual reality," *IEEE Trans. Wireless Commun.*, vol. 22, no. 7, pp. 4828–4842, Jul. 2023.
- [24] V. Va, H. Vikalo, and R. W. Heath, "Beam tracking for mobile millimeter wave communication systems," in *Proc. IEEE Glob. Conf. Signal Inf. Process. (GlobalSIP)*, 2016, pp. 743–747.
- [25] S. Jayaprakasam, X. Ma, J. W. Choi, and S. Kim, "Robust beam-tracking for mmWave mobile communications," *IEEE Commun. Lett.*, vol. 21, no. 12, pp. 2654–2657, Dec. 2017.
- [26] F. Liu, P. Zhao, and Z. Wang, "EKF-based beam tracking for mmWave MIMO systems," *IEEE Commun. Lett.*, vol. 23, no. 12, pp. 2390–2393, Dec. 2019.
- [27] J. Palacios, D. De Donno, and J. Widmer, "Tracking mm-wave channel dynamics: Fast beam training strategies under mobility," in *Proc. IEEE Conf. Comput. Commun. (INFOCOM)*, 2017, pp. 1–9.
- [28] K. Heimann, J. Tiemann, D. Yolchyan, and C. Wietfeld, "Experimental 5G mmWave beam tracking testbed for evaluation of vehicular communications," in *Proc. IEEE 2nd 5G World Forum (5GWF)*, 2019, pp. 382–387.
- [29] I. K. Jain, R. Subbaraman, T. H. Sadarahalli, X. Shao, H.-W. Lin, and D. Bharadia, "mMobile: Building a mmWave testbed to evaluate and address mobility effects," in *Proc. 4th ACM Workshop Millim. Wave Netw. Sens. Syst.*, 2020, pp. 1–6. [Online]. Available: <https://doi.org/10.1145/3412060.3418433>
- [30] Q. Zhang and C. Yang, "Testbed and performance evaluation of 3D MmWave beam tracking in mobility scenario," in *Proc. IEEE Conf. Comput. Commun. Workshops (INFOCOM WKSHPS)*, 2022, pp. 1–2.

[31] A. Marinišek, X. Cai, L. De Strycker, F. Tufvesson, and L. Van der Perre, "Impact of array configuration on head-mounted display performance at mm wave bands," in *Proc. Joint Eur. Conf. Netw. Commun. 6G Summit (EuCNC 6G Summit)*, 2023, pp. 192–197.

[32] R. Hersyandika, Q. Wang, Y. Miao, and S. Pollin, "User-movement-robust virtual reality through dual-beam reception in mmWave networks," in *Proc. IEEE Glob. Commun. Conf. (GLOBECOM)*, 2024, pp. 5271–5276.

[33] W. Tan, S. D. Assimonis, M. Matthaiou, Y. Han, X. Li, and S. Jin, "Analysis of different planar antenna arrays for mmWave massive MIMO systems," in *Proc. IEEE 85th Veh. Technol. Conf. (VTC)*, 2017, pp. 1–5.

[34] Y. Luo, J. A. Zhang, X. Huang, W. Ni, and J. Pan, "Optimization and quantization of multibeam beamforming vector for joint communication and radio sensing," *IEEE Trans. Commun.*, vol. 67, no. 9, pp. 6468–6482, Sep. 2019.

[35] *IEEE Standard for Information Technology—Telecommunications and Information Exchange Between Systems—Local and Metropolitan Area Networks—Specific Requirements—Part 11: Wireless LAN Medium Access Control (MAC) and Physical Layer (PHY) Specifications Amendment 3: Enhancements for Very High Throughput in the 60 GHz Band*, IEEE Standard 802.11ad-2012 (Amendment to IEEE Std 802.11-2012, IEEE Std 802.11ae-2012 IEEE Std 802.11aa-2012), 2012.

[36] *IEEE Standard for Information Technology—Telecommunications and Information Exchange Between Systems Local and Metropolitan Area Networks—Specific Requirements Part 11: Wireless LAN Medium Access Control (MAC) and Physical Layer (PHY) Specifications Amendment 2: Enhanced Throughput for Operation in License-Exempt Bands Above 45 GHz*, IEEE Standard 802.11ay-2021, 2021.

[37] "mmW-SDR: Accelerate your wireless innovations." TMYTEK. Accessed: Dec. 17, 2024. [Online]. Available: <https://tmytek.com/solutions/mmW-SDR>

[38] (AMD, Santa Clara, CA, USA). *Zynq UltraScale+ RFSoc ZCU111 Evaluation Kit*. Accessed: Dec. 17, 2024. [Online]. Available: <https://www.xilinx.com/products/boards-and-kits/zcu111.html>

[39] F. Minucci et al., "Building a real-time physical layer labeled data logging facility for 6G research," 2024, *arXiv:2410.01298*.

[40] X. Wang et al., "Millimeter wave communication: A comprehensive survey," *IEEE Commun. Surveys Tuts.*, vol. 20, no. 3, pp. 1616–1653, 3rd Quart., 2018.

[41] (Pharrowtech, Leuven, Belgium). *PTM1060 60 GHz Phased Array Antenna Module*. Accessed: Dec. 17, 2024. [Online]. Available: <https://pharrowtech.com/>

[42] "Oculus rift DK2." Xinreality. Accessed: Dec. 17, 2024. [Online]. Available: [https://xinreality.com/wiki/Oculus\\_Rift\\_DK2](https://xinreality.com/wiki/Oculus_Rift_DK2)

[43] "VIVE pro 2 headset." Vive. Accessed: Dec. 17, 2024. [Online]. Available: <https://www.vive.com/us/product/vive-pro2/overview/>



**RIZQI HERSYANDIKA** (Graduate Student Member, IEEE) received the B.Eng. degree in telecommunication engineering from the Bandung Institute of Technology, Indonesia, in 2010, and the M.Sc. degree in electrical engineering from the Delft University of Technology, The Netherlands, in 2016. He is currently pursuing the Doctoral degree with the Networked Systems – WaveCoRE Arenberg Group, Department of Electrical Engineering, KU Leuven, Belgium, and part of the H2020-MSCA-ITN MINTS project. He

also had working experience as a Spectrum Monitoring Engineer with the Ministry of Communication and IT Republic of Indonesia. His main research interests are mmWave communication, cell-free networks, spectrum management, and integrated sensing and communication.



**HAOQIU XIONG** (Student Member, IEEE) received the bachelor's degree in optoelectronic information science and engineering from the Harbin Engineering University in 2019, and the M.Sc. degree in electronic engineering from the Southern University of Science and Technology in 2022. He is currently pursuing the Ph.D. degree with the Networked Systems – WaveCoRE Arenberg Group, Department of Electrical Engineering, KU Leuven. His research interests include integrated sensing and communication, cell-free MIMO signal processing, and Wi-Gig sensing.



**YANG MIAO** (Senior Member, IEEE) received the M.Sc. and Ph.D. degrees from the Radio Propagation Laboratory, Mobile Communications Research Group, Tokyo Institute of Technology, Tokyo, Japan, in 2012 and 2015, respectively. From 2010 to 2015, she was a Research Assistant with the Takada Laboratory, Tokyo Institute of Technology. From 2015 to 2018, she was a Postdoctoral Researcher with the Institute of Information and Communication Technologies, Electronics, and Applied Mathematics, Universite Catholique de Louvain, Louvain-la-Neuve, Belgium, and IMEC, Wireless, Acoustics, Environment, and the Expert Systems Laboratory, Ghent University, Ghent, Belgium. From 2017 to 2018, she was a part-time Senior Antenna Engineer with Jaguar Radio Wave Corporation, Shenzhen, China. From 2018 to 2019, she was a Research Assistant Professor with the Southern University of Science and Technology, Shenzhen. From August 2019 to May 2024, she was an Assistant Professor. Since June 2024 she has been an Associate Professor with the Radio Systems Group, University of Twente, 4TU, The Netherlands. Since November 2021, she has been affiliated part-time with KU Leuven, Leuven, Belgium, as a Marie Curie Individual Fellow. Her research interests include joint communication and sensing, incorporating mobility, and human factors.



**QING WANG** (Senior Member, IEEE) received the Ph.D. degree from UC3M and IMDEA Networks Institute, Spain, in 2016. He is an Assistant Professor with the Embedded Systems Group, Delft University of Technology, The Netherlands. He is the Co-Founder of OpenVLC, an open-source and low-cost platform for VLC research. His research outcomes have been published at IEEE/ACM conferences and journals such as MobiCom, CoNEXT, SenSys, MobiSys, and ICLR. His research interests include visible

light communication & sensing, and embedded AI/TinyML for IoT and 6G. He has received nine paper awards, including the Best Paper Awards from WoWMoM'24, ICC'23, EWSN'23, SenSys'22, Morse'22, and COMSNETS'19, and the Best Paper Runner-Up Awards from EWSN'22, MobiCom'20 (Honourable Mention), and CoNEXT'16.



**SOFIE POLLIN** (Senior Member, IEEE) is a Professor with KU Leuven focusing on wireless communication systems. Before that, she worked with imec and the University of California, Berkeley. She is currently a Principal Member of the technical staff with imec. Her research centers around wireless networks that require networks that are ever more dense, heterogeneous, battery-powered, and spectrum-constrained. Her research interests are cell-free networks, integrated communication and sensing, and non-terrestrial networks.